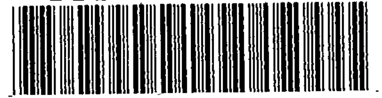
LINEAR LIBRARY
C01 0068 3231

Laser induced epitaxy of Ni and Co silicides

Brett R. Schroeder

University of Cape Town

Submitted in fulfilment
of the requirements for
the degree of Master of Science
at the
UNIVERSITY OF CAPE TOWN

September, 1994

The University of Cape Town has been given the right to reproduce this thesis in whole or in part. Copyright is held by the author.

The copyright of this thesis vests in the author. No quotation from it or information derived from it is to be published without full acknowledgement of the source. The thesis is to be used for private study or non-commercial research purposes only.

Published by the University of Cape Town (UCT) in terms of the non-exclusive license granted to UCT by the author.

University of Cape Town

Abstract

Laser annealing of metal layers on silicon substrates failed to produce uniform silicide layers. This can be attributed to constitutional supercooling effects. Laser annealing of thermally grown monosilicides gave low (~5%) minimum yields for Co and Ni on <111> substrates, as well as Ni on <100> substrates. The best yield achieved for Co on <100> substrates is 35%. The formation of a non-equilibrium epitaxial monosilicide was also achieved. Numerical calculations based on a heat flow approach gave fair quantitative agreement with experiment.

Acknowledgements

I am indebted to a number of people without whose assistance and guidance this work would not have been possible:

- Dr R. Pretorius and all the technical personnel at the Van de Graaf Group, NAC for all their support and assistance;
- My supervisor, Prof C.M. Comrie;
- The FRD for their financial assistance for the duration of this research;
- To the students and staff of UWC Physics department for their continued interest and encouragement during the past two years.
- To my loving wife, Vicki, for typing this thesis and for always being there for me.

Contents

1 Introduction **1**

1.1 Overview 1

1.2 Future Applications of Epitaxial Silicides 3

1.2.1 Metal Base Transistor (MBT) 3

1.2.2 Permeable Base Transistor (PBT) 4

1.3 Aims of the Research 5

2 Experimental Techniques **6**

2.1 Sample Preparation 6

2.2 Laser Annealing 7

2.3 Rutherford Backscattering Spectrometry (RBS) 9

2.3.1 Channeling 11

2.3.2 Experimental Setup 11

2.4 Scanning Electron Microscopy (SEM) 13

2.5 X-Ray Diffraction (XRD) 13

3 Laser Annealing **14**

3.1 Comparison of epitaxial growth techniques 15

3.2 Optical Absorption of Laser Radiation 17

3.3 Heat Transport 20

3.3.1 The Heat Flow Equation 20

3.3.2 Melting, Crystallisation and Undercooling 24

3.4 Numerical Method for Solving the Heat Flow Equation 30

4 Results and Discussion **34**

4.1 Metal on Silicon 34

4.2 Monosilicides on Silicon <111> and <100> substrates 40

4.3 Epitaxial Monosilicides 50

4.4 Co/Ni bilayers on <111> and <100> substrates 52

4.5 Results of Numerical Calculations 53

5 Conclusion **59**

A Green's Functions for the Heat Flow Problem **61**

B Optical Properties of Si; Ni, Co and their silicides at 694nm **64**

C Thermal Properties of Si; Ni, Co and their silicides **65**

D SEM Micrographs **67**

E Thermodynamics of the Ni–Si and Co–Si Systems **71**

Chapter 1

Introduction

1.1 Overview

Metal silicides have found applications since the early 1900's when they were first used as heating elements in electrical furnaces. During the 1950's these materials were used to protect rocket- and jet- engine parts made of tungsten or molybdenum from oxidation (due to the formation of an inert protective SiO_2 layer on the surface). Some of the transition metal (eg Cr) silicides are well suited to the fabrication of resistors because of their *high* electrical resistivity (due to their semi-conducting nature [1]) and relatively low temperature coefficient of resistivity. The interest in metal silicides as part of patterned electrical thin films in silicon integrated circuits came at the end of the 1970's when it was realised that with ever decreasing device dimensions, the resistance of conductors fabricated from polycrystalline silicon would become too high for effective use.

Metal silicides, which can be grown epitaxially on (and nowadays in) silicon, have been a topic of intensive research for more than a decade. The driving force for these investigations has certainly been the applications the metal silicides find in integrated circuit technologies. Because of their *low* electrical resistivity, high temperature stability and oxidation resistance; some of the transition metal silicides are extensively used either as ohmic contacts, gate electrodes, Schottky barriers or interconnects in integrated circuit devices. However, the research to date has not all been applied in nature — fundamental studies have been con-

[1]Some of the metal silicides are even found to be superconducting with small electron-phonon coupling constants and low (≈2K) transition temperatures.

ducted and will continue in an attempt to explain many unresolved properties and formation mechanisms of the silicides. A particularly important mechanism which remains unexplained is that of the Schottky Barrier Height (SBH) formation. Recent experiments have shown a large (400 meV) variation in SBH [1]; indicating a dependence on silicide crystallographic orientation, interface structure and substrate dopant while most recent Fermi-level pinning theories [2, 3] predict a constant SBH.

The formation of thin film metal silicides is usually achieved by the deposition of a metal layer on a single crystal silicon substrate followed by heating in a furnace until the desired silicide phase is produced. A reaction usually starts by formation of the metal-rich phase until all of the metal is consumed; further heating will then result in conversion to the silicon-rich silicides. These silicide layers are normally polycrystalline with grain sizes of about 1000Å. The metal silicides so formed are better suited to integrated circuit device applications than the previously used polycrystalline silicon but even these cannot match the characteristics of single crystal epitaxial silicides (which have lower electrical conductivity, better thermal stability and better reproducibility of interface properties than poly-silicides). However, the microcrystalline structure of thin silicide films depends on the method of film deposition and the conditions prevailing during film deposition and/or formation.

If there is an equivalence between the lattice symmetry of the silicide and that of the diamond lattice of silicon *and* the lattice spacing of the silicide is close to that of silicon; epitaxial growth of a silicide film onto the silicon single crystal can occur. The first silicide for which epitaxial growth was reported was PtSi [4] in 1967, which is surprising in view of the large lattice mismatch and different basic crystal structure. Silicon is cubic (diamond) with a lattice constant of 5.43 Å while PtSi is *orthorhombic* with lattice constants of 5.60; 5.93; 3.60 Å for a,b,c respectively. Since then epitaxial growth has been achieved for many different metal silicides on various crystallographic orientations of the Si substrate. Some of the silicides which have been grown epitaxially are $FeSi_2$, $TiSi_2$, $CoSi_2$, $NiSi_2$, Pd_2Si, YSi_2, $ErSi_{2-x}(0<x<0.5)$ and PtSi — comprehensive reviews of epitaxial silicides have been conducted by Chang [5]and Chen [6]. The possibility of growing many layers epitaxially on top of each other (heteroepitaxy) is bound to carry the design of integrated circuits over into three dimensions. However, since the prediction of epitaxial growth and epitaxy itself are both complex and still not well understood; the design of three dimensional structures will

still require a lot of empirical investigation.

1.2 Future Applications of Epitaxial Silicides

Currently most silicon-silicide contacts operate either as ohmic contacts or as Schottky barriers. In the ohmic contact role it has been suggested [7] that a buried silicide layer can be used as the collector contact of a bipolar transistor which would then have a cut off frequency of about 50 GHz. As a Schottky barrier the silicide is used as an *active* terminal of the devices. Two such possible devices which utilise this principle are the metal base transistor and the permeable base transistor.

1.2.1 Metal Base Transistor (MBT)

In a MBT the p-type base of a npn bipolar transistor is simply replaced by a metal base. The operation of a MBT relies on the injection of hot electrons from the emitter, through the base and into the collector. A schematic band structure diagram of an MBT is shown in Fig 1.1. The transit time of such a device is the time it takes charge carriers to diffuse "up and over" the emitter barrier at a thermal velocity, travel through the metal base at a saturated drift velocity v_d^{sat} and then pass "up and over" the collector barrier, also at v_d^{sat}. In order to keep the transit time to a minimum, it is firstly required that the metal layer be grown heteroepitaxially between the adjacent semiconductors. This will lead to a reduction in electron reflection at the interfaces as well as ensuring high Schottky barriers, which in turn result in low leakage currents.

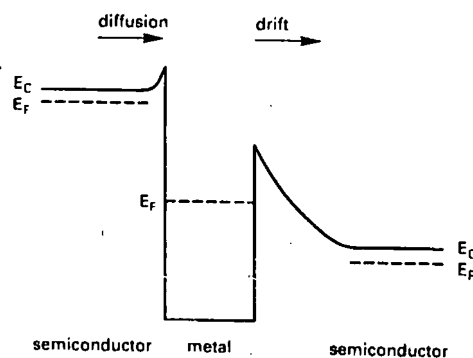

Figure 1.1: *Energy band diagram of a MBT.*

The silicides of nickel and cobalt seem to be most suitable for this purpose because of their low resistivity and small lattice mismatch with silicon. It is also necessary that the metal base be thin enough so that electrons may pass through the metallic layer without any energy loss i.e. the base thickness should be less than the mean free path of electrons in the material (64 Å in $CoSi_2$ [8]). To date, the two most common techniques used to produce these structures, mesotaxy[2] and molecular beam epitaxy, have been unable to meet this second requirement. However, even if this requirement is met in the future; it is still necessary for the electrons to overcome the base-collector potential barrier. As the electrons move from the metal, where $v_F \approx 10^6$ m s^{-1}, to the silicon, $v_F \approx 10^5$ m s^{-1}; a *large* portion of the kinetic energy is converted to potential energy. This large potential barrier causes most of the electrons to be quantum mechanically reflected at the interface. Despite these limitations a $CoSi_2$ MBT having a measured cut off frequency of 20 GHz, but low current gain, has been fabricated [9].

1.2.2 Permeable Base Transistor (PBT)

A PBT is made by replacing the continuous metal base of a MBT by a metal grid as shown in Fig 1.2. In the n type PBT shown electrons would flow from the n^+ emitter *between* the metal "fingers" of the grid and onwards to the collector, thus never actually passing *through* the metal. Since the metal grid is embedded in an n^- region a Schottky depletion layer is formed around each of these metal fingers. The size of this depletion layer and thus the current flow, can be controlled by the voltage applied to the grid. Complete "pinch-off" can then be achieved by suitably choosing the distance between adjacent fingers and the n^- doping concentration. Fig 1.2 also shows the energy levels across a PBT during "pinch-off" operation. Once again nickel and cobalt silicides are best suited for use as the grid material. However, Badoz *et al* [10] have successfully used WSi_2. PBT's have successfully been grown by a combination of MBE and CVD, mesotaxy through a mask and on pre-existing island structures on the silicon substrate. Since they are able to carry currents of up to 10^5A cm^{-2} and have cut off frequencies of $\sim$ 30 GHz, the most appropriate uses would be in high power and/or high frequency applications. The biggest advantage of PBT's is that the size of the

[2] A combination of *very* high dose ion implantation and high temperature annealing. See White *et al* *Appl. Phys. Lett.*, **50**, 95 (1987) for exact details of the process.

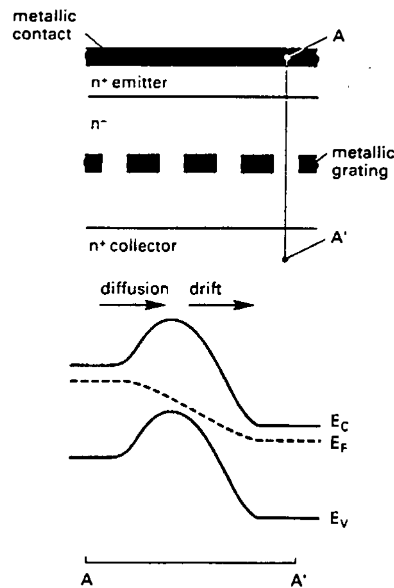

Figure 1.2: *Schematic cross-section of a PBT with the corresponding electron energy band diagram of an n-type PBT in pinch-off operation.*

control electrodes is determined by growth technology and *not* lithography, thus allowing for even smaller devices.

1.3 Aims of the Research

The fundamental aim of this research is to carry out a detailed comparison of the epitaxial characteristics of Ni and Co silicides formed by pulsed laser annealing. The nature of the comparison is, however, not to produce perfect Ni and Co silicides and then study their characteristics but rather to compare the epitaxial characteristics after each stage of the silicide production process. Differences in the response of Ni and Co to laser silicide formation will be noted mainly as functions of laser energy (density) and substrate orientation. These investigations will be carried out mainly through the techniques of Rutherford backscattering and ion beam channeling.

Chapter 2

Experimental Techniques

2.1 Sample Preparation

All experiments were conducted on commercially manufactured 3 inch single crystal silicon <111> and <100> wafers cut into 1cm^2 individual samples. No attention was paid to dopant type or concentration but the wafers had resisitivities in the 1–10 Ω cm range. The wafers were all chemically cleaned (acetone, methanol, rinsed in deionised water of resistivity greater than 10 MΩ cm), then dipped in a buffered 5% HF solution for 30 seconds and finally blow dried under high pressure nitrogen gas. After the cleansing process the wafers were loaded into an electron beam evaporation chamber (shown in Fig 2.1) which was subsequently evacuated. Samples spent about 10 minutes under atmospheric pressure after cleansing before being loaded.

All subsequent layers of material were deposited onto the silicon substrates (which were at room temperature) by means of electron beam evaporation at rates of 4–8 Å s^{-1}. The ambient pressure was $(1-4)\times10^{-7}$ Torr. Furnace annealing of the samples was performed in a Lindberg Sola Basic vacuum tube furnace at pressures less than or equal to 2×10^{-7} Torr. The furnace temperature could be varied in 1°C increments in the range from room temperature to 1000°C. It is estimated that the error on any non-room temperature reading is $\sim$ 20°C.

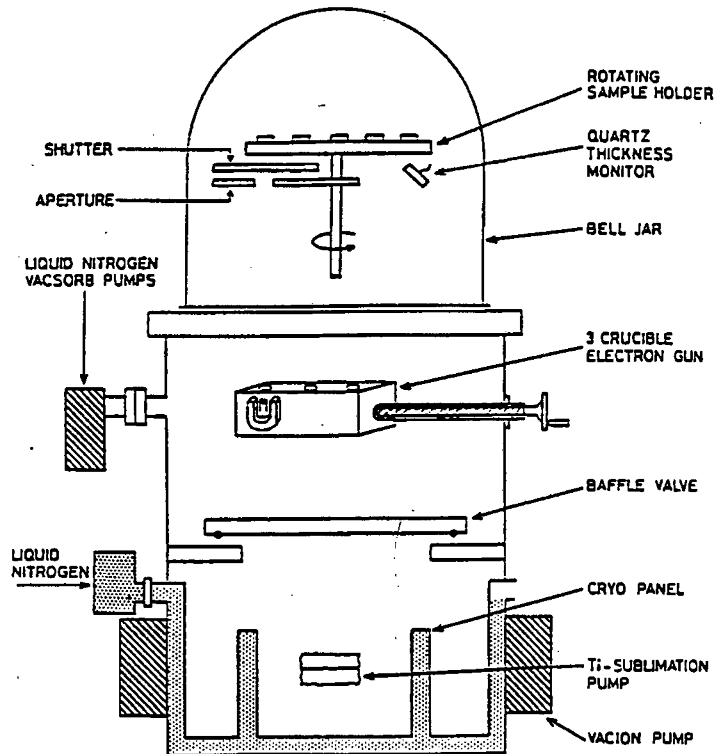

Figure 2.1: *A schematic representation of the High Vacuum electron beam evaporator. A Pfeiffer turbo molecular pump at the same height as the crucible is not shown.*

2.2 Laser Annealing

Laser annealing of samples was performed under atmospheric conditions using a Q-switched ruby laser supplied by JK Laser Ltd (System 2000). The laser had a wavelength of 694nm and pulse width of 30 nsec, while the output energy density could be varied continuously from 0.0 – 2.7 $\mathrm{J\,cm^{-2}}$. Fig 2.2 and Table 2.1 give an illustration and the technical details of the System 2000 respectively.

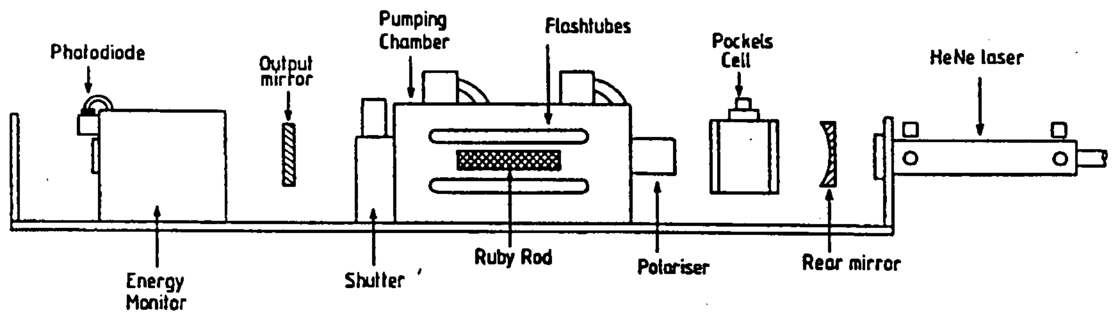

Figure 2.2: *Schematic of the pulsed ruby laser.*

Table 2.1: *Specifications of the pulsed ruby laser*

Wavelength	694 nm
Pulse width	30 nsec
Pulse energy	1.5 J
Peak power	50 Megawatts
Polarisation	Horizontal
Max. repetition rate	6 pulses per minute
Max. input voltage	2.01 kV
Pockels cell delay	570 μsec
Pockels cell voltage	2.5 kV

The pumping chamber of the laser consisted of a 9.5 mm diameter, 10 cm long ruby crystal and four parallel Xenon flash tubes that supplied the pumping power. Since the lasing efficiency of ruby is very temperature dependent (the efficiency decreases as temperature increases) the entire pumping chamber was cooled by flowing water. The coolant was thus brought into intimate contact with the entire ruby crystal and all of the flash tubes as well. Output power was varied only by varying the flash tube voltage.

Q-switching of the laser was provided by a self-contained sealed Pockels cell which had anti-reflection coated windows at both ends. The space between the end windows and the actual "Pockels crystal" was filled with an index-matching fluid (FC104) to minimise transmission losses.

The energy of each pulse was measured by diverting a small amount (about 8%) of the output beam, with a fused silica beamsplitter, to a photodiode. The current generated by the photodiode, after being integrated, then allowed the voltage generated by the diverted pulse to be displayed. The relationship between this output voltage and the laser energy is made linear by operating with a 15V reverse bias on the photodiode and limiting the maximum signal voltage to 1V.

The technique of Rutherford Backscattering Spectrometry (RBS) (see section 2.3) effectively gives an average of the lateral cross-section of the sample over the analysing beam area (1–2 mm in diameter). As a result it was necessary that the samples, after undergoing

laser annealing, were laterally uniform over an area at least as large as the RBS beam. The beam from any laser is usually Gaussian if operating in the TEM_{00} mode and even less uniform in any other mode. It was thus necessary to attach a beam homogeniser to the laser output. The homogeniser used was of the bent quartz tube type invented by Cullis *et al* [12]. The right angle bend of the homogeniser introduces phase and directional differences into various components of the laser beam; while the narrower output end of the homogeniser ensures that the energy density of the beam is not reduced by losses in the homogeniser itself. During irradiation the samples were placed less than 1 mm from the output end of the homogenising quartz tube. Ideally, the homogeniser should also have removed the time-varying non-uniformity of hot and cold spots caused by optical interference between the slightly different wavelengths of the output beam. However, this was not the case, especially at higher energies. After annealing at higher energies, non uniformities in surface colouration were often observed. These were usually in the form of small spots ($\approx \frac{1}{2}$mm in diameter) or larger semi-circular areas. Care was taken not to do any analysis in these regions but rather in areas representing the average sample structure.

2.3 Rutherford Backscattering Spectrometry (RBS)

Rutherford Backscattering Spectrometry (RBS) consists of collecting and analysing the ions that are scattered through angles greater than 90° if the incident beam is normal to the sample surface when the target material is bombarded with light ions having energies of the order of a few MeV. RBS can be described by the following physical processes, each one illustrating a particular capability or limitation of backscattering spectrometry:

1. The transfer of energy from a light projectile ion to a heavier target atom in an inelastic two-body collision. From momentum and energy conservation considerations the ratio of projectile energy after the collision to energy just before collision can be found. This ratio is termed the *kinetic factor* and is a function of projectile mass (M_1); target atom mass (M_2) and the angle through which the projectile is scattered (θ). Thus, for fixed M_1 and θ, RBS is able to distinguish between atoms of different mass M_2. The kinematic factor displays strongest dependence on M_2 when the scattering angle $\theta = 180°$. Therefore in order to obtain the greatest mass resolution, which is given by

Chu *et al* [13] as

$$\Delta M_2 = \frac{\Delta E}{E_o(4-\delta^2)(M_1/M_2^2)^2}, \tag{2.1}$$

a detector should be positioned as close as possible to the $\theta = 180^o$ position. In equation (2.1) ΔE is the energy resolution of the electronic detection system (20 keV in this case), E_o is the energy of the projectile beam before scattering and $\delta = \pi - \theta$. When detector angles greater than 179° are used it is also necessary to take into account the enhancement factor, first reported and explained by Pronko *et al* [14] and Crawford [15], which causes an increase in the expected number of particles scattered from the near surface region.

2. The probability that a scattering event will take place. Rutherford's formula for the differential scattering cross-section is invoked and thus a quantitative prediction of the expected number of backscattered particles is possible.

3. The energy loss of a projectile as it travels through a material. When the projectile is scattered at a depth x within the material rather than from a surface atom, it will lose kinetic energy through collisions with electron clouds both on its inward and outward paths through the material. This allows for the definition of a stopping cross-section

$$\varepsilon = \left(\frac{1}{N}\right)\left(\frac{dE}{dx}\right) \tag{2.2}$$

where N is the number of atoms per cm^3. A stopping cross-section factor, $[\varepsilon]$, may also be defined. Values of $[\varepsilon]$ are tabulated in reference [13] and are of the order of 100×10^{-15} eV cm^2 per atom. The total energy lost on the inward and outward paths, ΔE, can thus be obtained from

$$\Delta E = [\varepsilon] N x. \tag{2.3}$$

Alternatively, an energy loss factor $[s]$ can be defined and the energy loss is then given by $\Delta E = [s]x$. This approach, however, assumes knowledge of the density of the target material. Since the energy loss experienced by a projectile is independent of the atomic density of the target material, RBS does not really measure depth beneath the surface of a sample but rather the number of atoms per cm^2 encountered by the

incident beam: Any depth beneath the surface of a sample extracted from an RBS measurement implicitly assumes a full knowledge of the target material density. Bragg's rule for the additivity of cross-sections is normally assumed i.e. for a compound A_mB_n the stopping cross-section is given by $\varepsilon^{A_mB_n} = m\varepsilon^A + n\varepsilon^B$.

4. Since a particle traveling through a material loses energy in many individual collisions, the total energy loss for different particles (scattered from the same depth) will exhibit statistical fluctuations. This phenomenon, known as energy straggling, places a finite limit on the precision with which energy loses, and hence depths can be determined. The depth resolution of RBS is a few hundred Å for a normally incident beam but this can be improved by tilting the sample and/or the detector with respect to the beam direction. The total path length for scattering from any depth below the surface is then increased and this in turn produces an increase in the effective depth resolution.

2.3.1 Channeling

In channeling the incident ion beam is directed along an axial direction of the crystal whilst in the RBS technique described above the beam direction is random. The channeling effect arises because rows or planes of atoms can steer energetic ions by means of a correlated series of gentle, small angle collisions. Thus, in the case of a perfect crystal the incident beam only "sees" and undergoes Rutherford type collisions with the surface atoms. No such collisions occur with atoms at greater depths. This results in the number of backscattered particles being less than 5% of that detected in the case of a random beam direction. Channeling can be used to study the amount, and depth distribution, of lattice disorder. It may also be used to find the location of impurity atoms in lattice sites and to determine the composition and thickness of amorphous surface layers.

2.3.2 Experimental Setup

The samples were irradiated with 2 MeV $^4He^+$ particles accelerated by a Van de Graaf accelerator. The beam line was held under constant vacuum, while the pressure in the chamber containing the sample ladder and the silicon surface barrier detector was about 10^{-5} Torr. The detector, of solid angle 1.15 msr, was positioned such that particles scattered

through an angle of 165° would be detected. However, since the samples were mounted on a rotatable holder, scattering through small glancing angles could be carried out as well. All backscattering and channeling runs were halted after a total of 20 μC of charge had been collected. The analogue signal, amplitude proportional to energy, generated by the detector was passed through a preamplifier, amplifier, analogue-to-digital converter and finally sorted by a multichannel analyser. This digital information was then stored permanently for later access. A layout of the electronic equipment used for RBS and channeling is given in Fig 2.3.

Figure 2.3: *Schematic representation of the electronic layout used for RBS measurement. The solid lines indicate the electronics needed for RBS and the broken lines the additional electronics needed for channeling.*

The electronic equipment for channeling is similar to that used for RBS with the exception that the sample holder is replaced by a goniometer with three axes of rotation and a stepping motor accuracy of 0.01°. The rotations about the three axes could be remotely controlled from outside the vacuum chamber. In order to align, for instance the [111] direction of a Si$<$111$>$ crystal with the ion beam the following procedure was used: the z-axis was left at any random position and the y-axis set to zero. The x-axis was then scanned from $-5°$ to $+5°$. During this rotation a drop in yield was observed as the (111) plane became aligned with the incident beam. The position of the (111) plane was determined and then the x-axis set to this position. This was then repeated for the y-axis. The intersection of these "planes" then gives the $<$111$>$ axial direction. Once the $<$111$>$ axis of the crystal

was aligned with the beam, a backscattering spectrum was collected. This spectrum is subsequently referred to as the *aligned* or *channeling* spectrum. A *random* spectrum was also collected after moving the x-axis 2° and the y-axis through 7° in the positive direction.

2.4 Scanning Electron Microscopy (SEM)

All scanning electron microscopy was carried out on a Leica S440 SEM. Since the surface of the samples were non-conductive due to the presence of an oxide layer, the samples were first sputter coated with a layer of gold palladium alloy ($\sim$ 200Å). An accelerating voltage of 15 keV, probe current of 1 nA and a working distance of 13mm was used throughout. The samples were viewed directly from above i.e. no tilting towards the secondary electron detector was performed. However, secondary and backscattered electron images were recorded. Since the backscattered images were recorded in "compositional mode" the contrast in these images is derived from differences in atomic number. Thus if there are any lateral variations in surface composition, regions of high metal concentration will appear brighter because of the larger backscattering coefficient associated with heavier elements.

2.5 X-Ray Diffraction (XRD)

Since the only available diffractometer was of the $\theta - 2\theta$ type, XRD was unable to provide conclusive information about the epitaxial silicides. This was due to a combination of two factors (1) the epitaxial layers were very thin and thus did not produce large signals and (2) the signals that were produced were "swamped" by the silicon signal due to the very similar crystal structures and the epitaxial arrangement of the silicide on the silicon substrate.

Chapter 3

Laser Annealing

The first application of lasers that would become of interest to the semiconductor industry occured in the USSR when it was demonstrated that laser annealing of an ion implanted sample was able to remove the damage caused by the ion implantation process [11]. Since then lasers have found many semiconductor related applications, some of which are :

- the laser induced diffusion of thin dopant films deposited on the surface of samples and the incorporation of these dopants substitutionally at concentrations far exceeding the solid solubility limit;
- recrystallisation of doped amorphous films (deposited on single crystal substrates) into large grains or even single crystals;
- the removal of precipitates present after conventional high temperature dopant diffusion;
- formation of silicides from the deposited thin film metal layers;
- and even the formation of crystalline diamond from amorphous carbon films [16].

Some of the more device specific applications of laser annealing are :

- formation of Al-Si contacts on shallow junctions;
- formation of insulating layers of SiO_2, SiC or Si_3N_4 (in conjuction with ion implantation);

- prodution of silicide films for archival optical storage [77];
- formation of bipolar transistors with low base resistance (in conjunction with ion implantation);
- fabrication of short channel MOSFETs (due to minimal lateral spread of laser formed junction) [18];
- and reduction in the resistivity of polycrystalline silicon.

Even though the scope and variety of laser applications is wide, all of the above processes have collectively become known as *laser annealing.*

3.1 Comparison of epitaxial growth techniques

In practice ion implantation produces structures that are relatively shallow and does not produce the appropriate alloy composition required in many devices; thus, most epitaxial layers are fabricated by a deposition process. One of the most common of these deposition processes is chemical vapour deposition (CVD). In this process silicon and the dopant species are transported as hydrides or chlorides in the gas phase at atmospheric pressure. This gas stream then passes over heated single crystal substrates where chemical decomposition and epitaxial deposition occur. The composition of this layer can then be controlled by changing the relative flow rates of the gaseous species. CVD is a low cost process, can produce a wide variety of doping concentrations ($10^{13} - 10^{20}$ per cm^3), has deposition rates up to 1μm/min and the grown layers can be up to 100μm thick. These advantages have made CVD the workhorse of the semiconductor industry. However, CVD is only suitable for the growth of certain materials and does not produce very abrupt changes in material composition. This is mainly due to the finite gas flow velocities across the growing surface and the high substrate temperature (950–1200°C) required for chemical decomposition of the gases.

Most of these limitations can be overcome by molecular beam epitaxy (MBE) which is performed under ultra high vacuum (UHV) conditions, at lower substrate temperatures and uses monatomic gas transport species. The disadvantages of MBE are that it is a complex technique requiring a large initial capital investment, processing time per wafer is longer than that of CVD and the growth of device-quality material requires *very* careful substrate

preparation in order to eliminate the degrading effects of carbon contaminants and interfacial oxides. Some typical parameters of various thin film formation techniques are given in Table 3.1.

Table 3.1: *Typical Epitaxial Parameters*

Technique	Growth Rate (μm/min)	Thickness (μm)	Dopant concentration[a]	Substrate T (°C)	$\sqrt{Dt}$ (μm)
Ion implant	N/A	0.01–0.3	10	900[b]	0.01
CVD	0.1–1	0.1–100	1	950–1200	0.3
MBE	0.01–0.3	0.0001–10	1	450-900	0
Laser(solid)	10	0.001–1	10	RT–400	0
Laser(liquid)	10^8	0.001-1	1000	RT	0.3

[a] 1 = solid solubility
[b] For activation

In most experiments, laser epitaxy begins with a CVD- or MBE- like deposition but at a low (normally room) temperature. This low temperature deposition does not allow any diffusion and the resulting film is either amorphous or polycrystalline. The role of the laser is then to produce the one characteristic that has been sacrificed – perfect crystallinity. In contrast to the techniques discussed above, laser annealing offers the following advantages:

- can be performed in a variety of gaseous or vacuum environments, even in air;
- good control of the location of the heated area;
- selective heating of the near surface region without alteration of any nearby pre-existing structures;
- precisely controlled energies and high energy densities attainable;
- *much* shorter annealing times compared to furnace annealing;
- reduction in the concentration of interfacial impurities and
- the resulting epitaxy is not very sensitive to interface cleanliness [19].

The application upon which all further discussion of laser annealing will be based is that of silicide formation from deposited thin metal layers. It was first demonstrated in 1978 by Poate et al [20] that silicide layers could be produced by pulsed laser annealing of films of Ni, Pd or Pt on silicon substrates. The physical processes involved in laser annealing will be discussed in the following two sections.

3.2 Optical Absorption of Laser Radiation

Whilst the energy levels of nucleons are separated by energies of the order of keV or even MeV, electron energies are separated by only a few eV. And since average laser photon energies are typically $\approx$2eV, laser light impinging on a material interacts only with the electrons of that material. The absorption of energy from the incoming photons by the electrons of the material results in the excitation of bound electrons and/or excess kinetic energy of conduction band- and near Fermi surface- electrons. This excess energy is then transferred to the lattice in the following three steps:

1. Spatial randomization of the motion of the excited electrons. This takes place on a time scale of the order of the collision time ($\approx 10^{-14}$sec).

2. Equipartition of the energy i.e. sharing of energy between electron and lattice. This usually involves a large number of collisions and intermediate states. Several energy transfer mechanisms with varying characteristic time constants may be involved e.g. an excited electron in a semiconductor first loses energy by phonon emission in the conduction band and then once again upon recombination. Characteristic times for this process are $\approx 10^{-13}$sec in metals and $\approx 10^{-12} - 10^{-6}$sec (depending on the material and the intensity of the absorbed light) for non-metals. In this process energy is transferred to the lattice only in the region in which the light was absorbed.

3. Heat flow – the localised heat absorbed by the lattice in the above process is then transferred to the surrounding material.

Most documented optical properties of materials represent the response of bulk material to incident light that is usually weak and thus has no effect on the equilibrium state of the material. However, very intense laser beams *do* alter the properties of the material and

thus its subsequent response to incident radiation. These beam induced optical changes can usually be attributed to changes in the density and electronic properties; the generation of free carriers through inter-band transitions in semiconductors and the non-linear distortion of electron orbitals or whole molecules by intense electric fields. These mechanisms then manifest themselves through the following observable effects:

(i) Thermal Self Focussing of the incident beam – this occurs when the real part of the refractive index varies locally (i.e. across the beam width) as a function of irradiance. In some materials this occurs at powers as low as 1 Watt (laser power $\approx 10^7$ Watts).

(ii) Electric Field Self Focussing – under intense electric fields the linear relation between the electric field and the polarization breaks down. The dielectric function, and thus the refractive index, now becomes dependent on the local electric field experienced.

(iii) Free Carrier Effects become very important in semiconductors. The absorbed radiation causes electron-hole pairs to be generated which result in an increase in the absorption coefficient and a decrease in the reflectivity. These changed parameters now allow for more heat to be absorbed and thus more electron-hole pairs to be generated. This circular effect may result in "thermal runaway" or explosive material damage. Since the absorption cross section associated with pair generation is proportional to λ^2, this effect is most apparent when using infra-red lasers. Fig 3.1 demonstrates the large effect that electron-hole pair generation has on the surface temperature (the effect of an electron-hole concentration dependent band gap is also taken into account).

(iv) Reflection by hot metals : As the temperature of a metal increases the electron-lattice collision time decreases. A greater fraction of the electronic energy is then transferred to the lattice and is thus not re-emitted, causing a decrease in reflectivity and a subsequent increase in the energy absorption. This effect, however, does not lead to thermal runaway. Since metals are very reactive at high temperatures, reflectivity changes may occur due to chemical reactions at the surface (e.g.oxidation). Mechanical deformation may also cause changes in the reflectivity.

If a material is not single crystal and is inhomogeneous on a scale of $\approx \lambda$ then the optical properties may be modified by light scattering at grain boundaries or inclusions. Thin metal

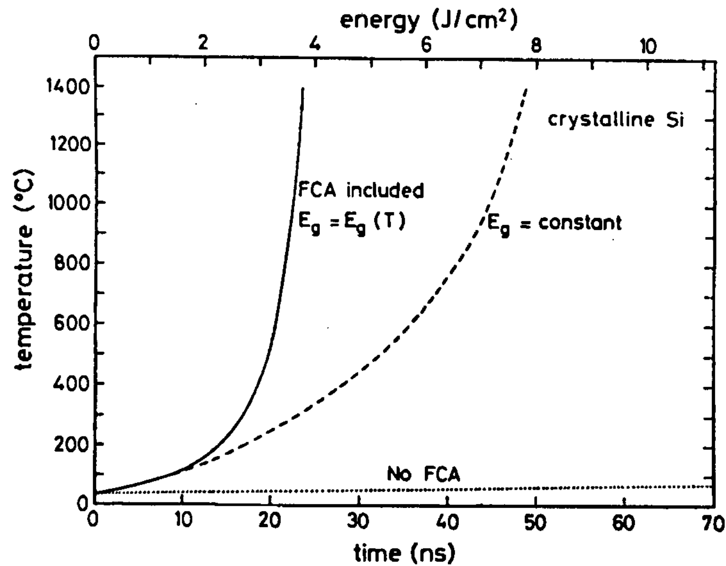

Figure 3.1: *Calculated surface temperature as a function of time for crystalline Si irradiated by a Nd-laser beam of 160 MW cm^{-2}. Different curves result if free carrier absorption (FCA) is ignored (dotted line) or included with a constant (dashed line) rather than temperature/e$^-$-h dependent band gap (A. Lietolla* et al*; J. Appl. Phys.,* **53***,3207 (1982))*

films may deviate from bulk behaviour due to "intrinsic" surface effects such as plasmon excitation or diffuse electron scattering. The optical behaviour of metal films is totally dominated by surface effects when the dimensions of the film are of the order of the optical absorption length [21].

The lack of detailed knowledge about the interaction of intense laser radiation with the optical properties of a semiconducting material resulted in two different and conflicting early models of the laser annealing process; each of which was able to explain some of the experimental data available at the time. Two of the most important results that needed explaining were the rise and fall in reflectivity during annealing and the spread in implanted dopant profiles. The "plasma model" [22] proposed that an electron-hole plasma was produced by the incident radiation and this caused the formation of a "plasma-fluid" state. The "melting/thermal model" [23, 24] proposed that the radiation absorbed in the near surface layer was converted to heat which then diffused throughout the material. If the amount of heat generated was sufficient the surface layer of the material melted and the liquid-solid interface (cf. melt front) would initially move deeper into the material as more of the solid began melting. The melt front would eventually reach a maximum depth when the heat supplied

by the laser and/or heat flow from the liquid was no longer sufficient to overcome the latent heat of fusion. At this stage, as heat continued to flow into the cooler, deeper regions of the substrate, the deepest regions of the liquid would begin to solidify; thus causing the melt front to start moving towards the surface. The melt front would continue on its path towards the surface until all the liquid had resolidified. The remaining heat would then diffuse through the solid until the ambient temperature had been achieved. The method of recrystallisation from the liquid phase and the distribution of atoms within the liquid ultimately determine the characteristics of the "laser grown" material. Even in regions that have not melted the material properties may be altered as well – partial solid-state recrystallisation of ion implanted silicon has been demonstrated [25]. It is now generally accepted that the *thermal model* is correct in view of the following evidence :

(i) the calculations of [23] and [24] agree with measured melt lifetimes, melting thresholds, etc.;

(ii) it was theoretically shown [26] that an electron-hole plasma created by nanosecond laser pulses would not be dense enough to induce a plasma-fluid phase in silicon that would last for about 100 nanoseconds (the measured duration of increased reflectivity);

(iii) a measured increase in electrical conductance of Si during annealing due to a metallic liquid phase being present [27] and

(iv) the transient conductance experiments of Galvin *et.al* [27] measured recrystallisation velocities that agreed with the calculations of [23] and [24] to within a few percent.

The thermal model has been developed in detail by Wood in a series of three excellent articles ([28],[29] and [30]) that cover heat flow, dopant diffussion and non-equilibrium segregation effects in detail.

3.3 Heat Transport

3.3.1 The Heat Flow Equation

Consider a slab of material of thickness L that is positioned between the planes $z = 0$ and $z = L$ (this includes the semi-infinite solid for which $L = \infty$). The laser beam which is

taken to be cylindrically symmetric, is incident upon the $z = 0$ plane. Thus the $x - y$ plane coincides with the surface plane of the sample. Since the $x - y$ dimensions of the sample (≈1cm) far exceed those in the z direction (≈100μm) and only heat flow perpendicular to the surface is of interest; a one dimensional treatment shall suffice. The initial temperature of the sample is taken as being 0 K — but any uniform initial temperature may simply be added to a calculated temperature. The mathematical theory of heat conduction is based on the assumption that the heat flux Φ across a plane at a depth z_o in the sample is given by $\Phi(z_o) = -K\,(\nabla T)_{z_o}$. Assuming this to be true, one can then express the energy (per cm^2) balance for a slab of material situated between z and $z + \Delta z$ in finite difference form as follows

$$[\Phi(z) - \Phi(z + \Delta z)]\,\Delta t = \rho\,\Delta z\,C\,\Delta T \tag{3.1}$$

where ΔT is the change in temperature due to a net heat flux across the boundaries of the region. Letting Δz $\to$ 0 then allows one to obtain the usual one dimensional differential heat diffusion equation. If a source term (along with its spatial and temporal dependences) is included then an equation describing the laser annealing process is obtained

$$\frac{\partial T}{\partial t}(z,t) = \frac{1}{\rho C}\frac{\partial}{\partial z}\left(K\frac{\partial T}{\partial z}\right) + \frac{(1-R)}{\rho C}\alpha I_o(t)e^{-\alpha z} \tag{3.2}$$

where $I_o(t)$ is the incident laser pulse energy density (J cm^{-2}).

ρ the mass density of the material (g cm^{-3})

C the specific heat capacity (J g^{-1} K^{-1})

K the thermal conductivity (W cm^{-1} K^{-1})

R surface reflectivity at the laser wavelength

α the optical absorption coefficient (cm^{-1})

z the depth below the surface of the material (cm).

Strictly T is a function of (x, y, z, t). Equation (3.2) is based on the implicit assumption that Δz can be made arbitrarily small. In doing this, the finite mean free path d of the heat carriers (electrons and/or phonons) has been neglected. Harrington [31] has shown that in metal most of the heat flux across any given plane is carried by electrons that had their last

collision with the lattice within a few mean-free paths of the given plane. This means that the heat flux follows the local temperature gradient only if ∇T is constant over a distance of several mean-free paths. If this is not so then it means that a significant fraction of the heat is then carried by particles that "remember" a different temperature gradient. If one assumes that Δz may not be less than, say, $10d$; it is not necessarily true that the finite differences in equation (3.1) can be replaced by differentials. If the flux difference term is expanded in terms of a Taylor series about z then it is seen that the "linear" heat diffusion equation is valid only if

$$5d\left|\frac{\partial^3 T}{\partial z^3}\right| \ll \left|\frac{\partial^2 T}{\partial z^2}\right|. \tag{3.3}$$

If not, then higher order spatial derivatives must be retained to calculate the temperature distribution correctly. The requirement of a temperature gradient constant over several mean-free paths may be violated for short times during laser annealing. Equation (3.2) then overestimates the heat flux away from the surface and underestimates the surface temperature. Despite all these hidden non-linearities [1], it has been shown that "linear" heat conduction theory is valid for most laser annealing applications (for instance, see the calculations in [23]and [24]).

In order to obtain the temperature distribution as a function of time and position it is necessary to solve equation (3.2) subject to the appropriate boundary conditions. These boundary conditions are that $\frac{\partial T}{\partial z} = 0$ for $z = 0$ and $z = L$ at all times. It is also implicitly assumed that the generated heat density in the material is equal to the energy density of the laser beam. The Greens function technique, which has been covered in detail in the literature [33], is easily adapted to the laser heating problem. The general approach is as follows : the Greens function G allows the temperature distribution produced by an "instantaneous" heat source of unit energy to be calculated (G has dimensions of $K.J^{-1}$). Once G is known, the temperature distribution for a continuous heat source of power

$$P_a(t') = (1 - R)\iint I(x', y', t')\, dx'dy' \tag{3.4}$$

[1]Kim *et.al* [32] have presented a general analytic technique for dealing with non-linear heat (and mass) diffusion

can then be found from

$$\boxed{T(x,y,z,t) = \int_0^t P_a(t')\, G(x,y,z,x',y',z',t-t')\, dt'} \tag{3.5}$$

where x, y, z, t and x', y', z', t' are the coordinates of the field and source points respectively. Appendix A covers the Greens function technique in more detail and also gives the appropriate Greens function for various physical situations. For notational convenience the heat diffusivity $D = K/\rho C$ and the heat diffusion length $\delta = 2\sqrt{Dt}$ will be introduced.

Even though the Greens function technique is fairly simple in its approach, very few closed solutions can be obtained for the heat flow problem. A case for which a closed solution *does* exist is that of a beam homogenised laser (i.e. laterally uniform source). To arrive at this solution it is also necessary to assume temperature independent thermal (K, C) and optical (α, R) parameters, infinite sample thickness $(L = \infty)$, a laser beam that is constant in time, that the laser does not induce a phase change in the material and that there is no inhomogeneity of the sample along the z axis. The solution is then given by

$$\begin{aligned} T(z,t) &= \frac{(1-R)I}{K}\left[\delta\ ierf(z/\delta) - \frac{1}{\alpha}e^{-\alpha z}\right. \\ &\left. + \frac{1}{2\alpha}e^{(\alpha\delta/2)^2}\left\{e^{-\alpha z}\, erfc\left(\frac{\alpha\delta}{2} - \frac{z}{\delta}\right) + e^{\alpha z}\, erfc\left(\frac{\alpha\delta}{2} + \frac{z}{\delta}\right)\right\}\right] \end{aligned} \tag{3.6}$$

while the time dependence of the surface temperature is described by

$$T(0,t) = \frac{(1-R)I}{K}\left[\frac{\delta}{\sqrt{\pi}} - \frac{1}{\alpha}\left\{1 - e^{(\alpha\delta/2)^2}\, erfc(\alpha\delta/2)\right\}\right]. \tag{3.7}$$

To include cooling of the sample after the completion of the laser pulse it is necessary to extend the integration in equation (3.5) to times longer than the pulse duration. However, analytical solutions to this problem exist only in the simplest of cases (e.g. a uniform source along with an infinite absorption coefficient).

The Greens function approach to solving the heat flow problem rests on the unrealistic assumption of temperature-independent material properties. The expressions that can be derived through this approach are adequate to reproduce the essential features of the temperature distribution, but no more than qualitative agreement can be expected with

experimental results. Usually both the thermal conductivity and specific heat are strong functions of temperature. Another limitation of the Greens function technique is that it is unable to take into account phase transitions involving latent heats (i.e. melting and solidification). It is for these reasons that a *numerical approach* to heat flow has to be sought in order to gain a better understanding of the laser annealing process. Such a numerical approach will be outlined in section 3.4.

3.3.2 Melting, Crystallisation and Undercooling

Since the state of the final material is usually not affected by the inward motion of the liquid - solid interface all further attention will be paid only to the outward motion of the melt front (i.e. from its deepest position and then along its path towards the surface). The movement of the melt front is governed by two competing physical processes; namely kinetics (how quickly and efficiently the atoms of the liquid can attach themselves to the solid) and heat flow (how quickly the resultant latent heat can be drawn away). The slower of these processes will then always limit the propagation of the melt front. The thermodynamic driving force for the propogation of the melt front is the lowering in Gibbs free energy (per gram) achieved by going from a liquid to a solid phase at $T < T_m$. This change in energy is given by

$$\begin{aligned} \Delta G_{sl} = G_s - G_l &= H_s - H_l - TS_s + TS_l \\ &= \Delta H_{sl} - T\Delta S_{sl} \end{aligned} \tag{3.8}$$

where H and S are the enthalpy and entropy per gram respectively (assuming equal densities for liquid and solid). At the equilibrium melting temperature T_m, ΔG_{sl} is zero by definition. Thus, ΔG_{sl} may be approximated by substituting $\Delta S_{sl} = \Delta H_{sl}/T_m$ into equation (3.8) and obtaining

$$\Delta G_{sl} \approx \Delta H_{sl}\frac{(T_m - T)}{T_m} = \frac{\Delta H_{sl}\Delta T}{T_m} \tag{3.9}$$

Strictly speaking the substitution for ΔS_{sl} only holds at $T = T_m$ but equation (3.9) will be used as an estimate for ΔG_{sl} when $T \neq T_m$. From the definition of the quantities in equation (3.8) it can be seen that ΔH_{sl} is a negative quantity and for $T < T_m$ then ΔG_{sl} is less than zero as well.

The standard theories of crystal growth from a melt [34, 35] usually express the velocity of a liquid-solid interface as the difference between the forward [2] and reverse [3] kinetic rate constants. If these two rates are unequal then a movement of the liquid-solid interface occurs. A treatment of this sort usually leads to an expression of the following kind

$$v = aA\nu_i \left[1 - e^{\Delta G_{sl} M / RT_i}\right] \tag{3.10}$$

where a is the interatomic spacing in the growth direction, A is the accommodation probability, ν_i is a thermally activated jump frequency and M is the molar mass of the solid. A can be interpreted as the fraction of sites at the interface where attachment of a new atom is energetically favourable. The expression outside the brackets in equation (3.10) is usually composed of two terms, a distance which the interface moves per solidification event (e.g. one monolayer) and a rate at which these events occur. The exact form of this expression depends on the atomic mechanism model chosen to represent solidification; for example, Broughton *et al.* [36] used the thermal velocity of atoms in the liquid to obtain a frequency term. For most metals at all temperatures, $A \sim 1$ while for semiconductors A is small and anisotropic — being smallest for densely packed interface directions. This makes growth along a <100> direction in a cubic crystal faster than growth along <111> direction [37]. The jump frequency generally exhibits very strong temperature dependence and is of the order of 10^{13} sec^{-1} for pure metals. In the solidification of molecular or covalently bonded materials coordination of the motion of several atoms is required as opposed to jumps of single atoms. Thus, the growth of these compounds is slower than that of metals. The growth of a *compound* crystal from a *binary* melt is more complicated, particularly if the crystal and melt have different compositions. Jackson [38] has considered this case, and concluded that an equation of the form of equation (3.10) is still valid but with an appropriate driving force replacing ΔG_{sl}. The jump frequency can then be replaced by the frequency for diffusive transport in the melt

$$\nu_i \sim D/a^2$$

where D is the melt diffusivity at the interface ($\sim 10^{-4}$cm^{2}s^{-1}). For metallic compounds ν_i

[2] atoms moving fom liquid to solid

[3] atoms moving from solid to liquid

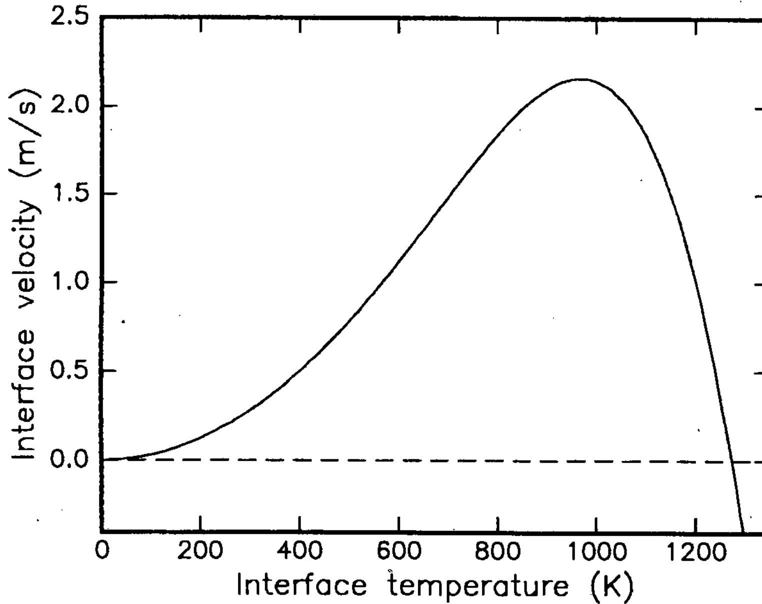

Figure 3.2: *Interface velocity as a function of temperature for NiSi (T_m = 1273 K). A jump frequency of $\nu_i = 10^5 T^2$ was used in order to represent the essential features of such a curve. Exact knowledge of ν_i is obviously limited.*

is of the order of 10^{11} sec^{-1}. A plot of the interface velocity as a function of the temperature, T, is given in Fig 3.2. Note that for small undercooling i.e. $|\Delta G_{sl} M| \ll RT$, the interface velocity is proportional to the undercooling. At large undercoolings the term in brackets in equation (3.10) tends to unity and the velocity is then governed by the temperature dependence of the jump frequency. From equations (3.9 and 3.10) it can be seen that if T is equal to the equilibrium melting temperature, then the interface velocity is zero. A necessary requirement for the movement of the interface towards the surface is thus the undercooling of the liquid.

The interface velocity can also be obtained by considering the heat flow budget across the moving interface. The heat flux in the solid away from the interface J_s must be balanced by the heat (flux) flowing from the liquid into the solid J_l plus the rate at which latent heat is being generated at the interface, $-v\Delta H_{sl}\rho$ (since $\Delta H_{sl} < 0$). This balance can then be written as

$$J_s = J_l - v\rho\Delta H_{sl}$$

$$v\rho\Delta H_{sl} = K_s\left(\frac{\partial T_s}{\partial z}\right)_i - K_l\left(\frac{\partial T_l}{\partial z}\right)_i \qquad (3.11)$$

where the subscripts s,l and i refer to the solid, liquid and the interface respectively. The thermal gradient in the liquid is usually much less than in the solid and thus the second term in equation (3.11) may be neglected, giving

$$v \approx \frac{K_s}{\rho \Delta H_{sl}} \left(\frac{\partial T_s}{\partial z} \right)_i \tag{3.12}$$

The interface velocity is thus seen to be proportional to the difference in the temperature gradients or approximately directly proportional to the temperature gradient in the solid. No dependence on the undercooling is obtained by this approach and it is usually assumed that the interface is at the equilibrium temperature T_m. It is convenient to ignore the kinetics, or equivalently to assume "infinitely fast" kinetics i.e. the material is able to change phase instantaneously at a fixed temperature irrespective of the interface velocity. This assumption has implicitly been made in most calculations of the interface velocity [28, 23]. For a calculation that does allow for finite interface kinetics see reference [39].

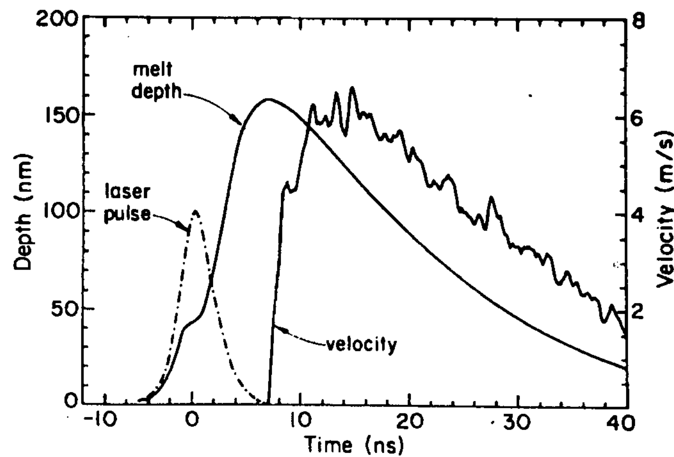

Figure 3.3: *Melt depth versus time as measured by the electrical conductance technique for 3.5 ns ruby irradiation of silicon. The solidification velocity is the numerical derivative of the melt depth data. (Galvin* et al; Appl. Phys. Lett., **46**, *644 (1985))*

The interaction between the processes of heat flowing away from the interface and the attachment of atoms to the solid at the interface then determines the actual interface velocity. The melt front will always move at the *slower* of the two possible velocities i.e. either the "kinetic" velocity of equation (3.10) or the "thermal" velocity of equation (3.12). Figure 3.3 shows a plot of the interface position and velocity as a function of time (during solidification only). At the onset of solidification, $v = 0$; thus no latent heat is released at the interface

and the flux out of the liquid J_l equals the flux through the solid J_s. If no further energy is supplied by the laser then the liquid temperature will be reduced. This reduction in liquid temperature undercools ($T_{liq} < T_m$) the interface region and solidification begins at a velocity given by equation (3.10). In the initial stages of solidification the heat released $\rho v|\Delta H_{sl}|$ at the interface is insufficient to balance J_s (due to the large thermal gradients). Thus, more heat is extracted from the liquid thereby increasing the undercooling $\Delta T = T_m - T_i$ further. As the undercooling increases the velocity increases until $\rho v|\Delta H_{sl}| = J_s$, then at this stage $J_l = 0$ and the liquid does not undercool further. During this transient i.e. from $v = 0$ to $\rho v|\Delta H_{sl}| = J_s$ (where the velocity is a maximum) the velocity of the interface is determined by the response of the interface to the undercooling and described by equation (3.10). This is referred to as the interface controlled regime or the velocity is said to be interface limited. After this initial transient up to the maximum velocity, the heat released by solidification is sufficient to balance the flux "required" by the temperature gradient in the solid, thus causing the degree of undercooling to decrease as well. As the temperature gradient at the interface decreases (slowly) in time, the velocity decreases accordingly. Thus, the interface velocity is now heat flow limited and described by equation (3.12).

During interface limited growth the thermal gradients are very large which then allow for a large "thermal" interface velocity. However, the atoms in the liquid are unable to successfully attach themselves to the solid at an equivalent rate and this then limits the propagation of the interface. During heat flow limited growth the atoms are able to attach themselves to the solid "quickly enough" but the solid is then unable to carry away the resulting latent heat because of the smaller temperature gradients present. Spaepen and Turnbull [40] have presented a general method that allows the following rule/guide to be established

Large Undercooling $\Rightarrow$ Interface Limited Growth
Small Undercooling $\Rightarrow$ Heat Flow Limited Growth

Since at the point of maximum velocity, i.e. at the point of changeover from interface to heat flow limited growth, the maximum "permitted" interface velocity must equal the maximum "permitted" heat flow velocity; the following method of approximating the maximum undercooling ΔT_{max}, which occurs at the maximum velocity, is proposed. Equations (3.10)

and (3.12) are set equal to each other and the usual approximation about ΔG_{sl} is made according to equation (3.9) with ΔT_{max} now replacing ΔT. The following expression is then obtained

$$\frac{K_s}{\rho \Delta H_{sl}} \left(\frac{\partial T_s}{\partial z} \right)_i = a A \nu_i \left[1 - e^{\Delta G_{sl} M / R T_i} \right] \tag{3.13}$$

where it is implied that the thermal gradient and attachment frequency are those at the point of maximum velocity, then

$$\frac{M \, \Delta G}{R T_i} = ln \left[1 - \frac{K_s}{a A \nu_i} \left(\frac{\partial T_s}{\partial z} \right)_i \frac{1}{\rho \Delta H_{sl}} \right] \tag{3.14}$$

$$\frac{\Delta T_{max}}{T_i} = \frac{R T_m}{M \, \Delta H_{sl}} ln \left[1 - \frac{K_s}{a A \nu_i} \left(\frac{\partial T_s}{\partial z} \right)_i \frac{1}{\rho \Delta H_{sl}} \right]; \tag{3.15}$$

if the right hand side is now set equal to X say, then the following simple expression may be derived

$$\boxed{\Delta T_{max} = \left(\frac{X}{1 + X} \right) T_m} \tag{3.16}$$

where

$$X = \frac{R T_m}{M \, \Delta H_{sl}} ln \left[1 - \frac{K_s}{a A \nu_i} \left(\frac{\partial T_s}{\partial z} \right)_i \frac{1}{\rho \Delta H_{sl}} \right] \tag{3.17}$$

Equation (3.16) will only provide an estimate of the maximum undercooling because of the uncertainties in the thermal gradient $\partial T_s / \partial z$ and the successful attachment frequency $A \nu_i$. However, a measurement of the maximum interface velocity will allow the thermal gradient to be obtained fairly accurately from equation (3.12). From equations (3.16) and (3.17) it can be seen that insignificant undercooling ($\Delta T < 1K$) will occur when $X < 10^{-3}$. This implies that for small ΔT the argument of the natural logarithm in (3.17) must be > 0.99 or equivalently that

$$\left| \frac{(\partial T_s / \partial z)_i}{A \nu_i} \right| < 10^{-6} \tag{3.18}$$

since the absolute value of $K_s / a \rho \Delta H_{sl}$ is of the order of 10^4 for most materials (see Appendix C). Although ν_i exhibits a very strong dependence on the interface temperature it would not vary by more than one order of magnitude during the undercooling. The thermal gradient

in the solid, however, varies by several orders of magnitude during annealing and is thus the most important parameter in determining the magnitude of the resultant undercooling. Once again it is noted that for small undercoolings the motion of the interface will be limited by heat flow due to small thermal gradients.

3.4 Numerical Method for Solving the Heat Flow Equation

The most important advantage that a numerical approach to solving equation (3.2) offers over an analytical approach is that the temperature dependence of the thermal and optical parameters may accurately be taken into account. The following algorithm was implemented in Fortran 77 and calculations were carried out on a VAX 11-750.

The sample was divided into slices of thickness Δz each and the time into a finite number of intervals Δt. It was found that a total sample thickness of approximately 50 000Å was sufficient to simulate an actual sample thickness of 380μm. In the ith layer, where the deepest side is at a depth of $i\Delta z = z_i$, the energy absorbed from the laser pulse during the time interval Δt is

$$\Delta Q_i^{(a)} = I(z_i, t)\left[1 - e^{-\alpha\Delta z}\right]\Delta t \tag{3.19}$$

where power density at the depth z_i at a time t is given by

$$I(z_i, t) = (1 - R)I_o(t)e^{-\alpha z_i}. \tag{3.20}$$

The amount of heat received by the ith layer due to thermal diffusion from the two adjacent sides is

$$\Delta Q_i^{(d)} = \left[K_L \frac{T_{i-1} - T_i}{\Delta z} + K_R \frac{T_{i+1} - T_i}{\Delta z}\right]\Delta t \tag{3.21}$$

where T_i is the temperature of the ith slice and K_L and K_R are the thermal conductivities at the two boundaries of the slice, which are "averaged" as follows

$$K_L = \frac{1}{2}\left[K(T_{i-1}) + K(T_i)\right]$$

$$K_R = \frac{1}{2}\left[K(T_i) + K(T_{i+1})\right] \tag{3.22}$$

The temperature rise ΔT_i is given by

$$\begin{aligned} \Delta T_i &= T_i(t+\Delta t) - T_i(t) \\ &= \frac{\Delta Q_i^{(a)} + \Delta Q_i^{(d)}}{\rho C \Delta z}. \end{aligned} \tag{3.23}$$

When the temperature reaches the melting point T_m, ΔT_i is set equal to zero and the amount of heat $\Delta Q_i^{(a)} + \Delta Q_i^{(d)}$ received in subsequent time intervals is used to melt the layer according to the latent heat of fusion. The temperature is then allowed to rise again only once the entire i^{th} layer has melted. This is achieved by defining the quantity

$$\Delta Q_i' = \Delta Q_i^{(a)} + \Delta Q_i^{(d)} - (T_m - T_i(t))\,\rho C \Delta z \tag{3.24}$$

which then represents the energy available for melting the ith layer (if $T_i(t) \leq T_m$) or the energy being liberated during solidification (if $T_i(t) > T_m$). Thus, the fraction of the ith layer that has melted or solidified during the time Δt is given by

$$\Delta FF_i = \frac{\Delta Q_i'}{\Delta H \rho \Delta z} \tag{3.25}$$

where $\Delta H = |\Delta H_{sl}|$. The new value of the molten/solidified fraction can now be calculated according to $FF_i(t+\Delta t) = FF_i(t) + \Delta FF_i$. The variable FF_i then offers a means of controlling the temperature during melting/solidification through the following subalgorithm

- if $0 \leq FF_i(t+\Delta t) \leq 1$, then $T_i(t+\Delta t)$ is set equal to T_m,
- if $FF_i(t+\Delta t) > 1$, then $FF_i(t+\Delta t)$ is set equal to 1 and the quantity $\Delta Q'' = (FF_i(t+\Delta t) - 1)\rho \Delta H \Delta z$ is calculated,
- and if $FF_i(t+\Delta t) < 0$, then the quantity $\Delta Q'' = FF_i(t+\Delta t)\rho \Delta H \Delta z$ is calculated.

The quantity $\Delta Q''$ is then the heat available for varying the temperature after complete melting or solidification of the layer has occurred. Finally the temperature

$$T_i(t+\Delta t) = T_m + \frac{\Delta Q''}{\rho C \Delta z} \tag{3.26}$$

may be calculated. In this approach the liquid-solid interface is always at the equilibrium melting temperature T_m.

This computation procedure is then applied to all subsequent layers of the sample. Once the computation of $T_i(t + \Delta t)$ is complete for all the layers; the value of t is incremented by Δt and the whole computation procedure begins again for all layers. Calculations were performed subject to the following boundary conditions

- initial sample temperature of 300K at all depths,
- $T = 300$K for any depth greater than 50 000Å and
- there is no heat loss from the sample to the surroundings due to thermal conduction or radiation. Wood *et al* [28] have shown this to be a very good assumption because the times involved are too short for these losses to become significant.

The disadvantage of such a code is that in order to obtain good spatial resolution it is necessary to have very small time steps Δt. This leads to computation times of the order of 36 hours on the VAX 11-750 that was used. The maximum size of the time steps can be obtained from the stability criterion for solving parabolic partial differential equations [41]

$$\Delta t < \frac{1}{2}(\Delta z)^2 \left(\frac{\rho C}{K}\right)_{minimum} . \tag{3.27}$$

Thus for a slice thickness of 100Å, time steps of 0.0005 nsec were used when simulating radiation of silicides on a crystalline silicon substrate. The reason for this condition stems from the fact that the finite-difference equation has solutions which do not satisfy the original differential equation (3.2). Only those solutions of equation (3.23) which also satisfy the stability criterion always remain real and finite.

The program was used to simulate the laser annealing of a metal or metal silicide layer on a single crystal silicon substrate. Appendices B and C contain the optical and thermal parameters that were used in these calculations. Due to the scarcity of temperature dependent expressions for some of the parameters (especially those of the silicides) room temperature values were used as substitutes in the calculations where necessary. It is believed that due to the very short duration of interface limited growth compared to that of heat flow limited growth (see Fig 3.3), a heat flow approach will represent the physical situation

very closely. Perfect agreement with experiment is, however, not expected as the program has limitations and must makes some assumptions, the most important of these being:

- No undercooling is taken into account and thus $T_i = T_m$ at all times. Wood and Geist [42] have developed a method that allows the undercooling (and even nucleation events) to be taken into account.
- No intermixing/diffusion of different materials in the liquid phase is considered. Thus, the calculations of this work (i.e. metal or metal silicides on silicon) will be most accurate when only the surface material melts or a very small amount of the substrate melts along with the surface layer.
- A gaussian temporal profile for the laser beam is assumed. This is not necessarily true; the pulse shape may even vary from pulse to pulse.
- It is assumed that the laser beam is perfectly uniform laterally.

The results of calculations carried out using the above algorithm will be presented in the following chapter.

Chapter 4

Results and Discussion

4.1 Metal on Silicon

As a first attempt at forming an epitaxial silicide, nickel layers of 300, 600 and 900 Å thickness were deposited onto silicon <111> wafers as described in section 2.1. These were then removed from the evaporation chamber and laser annealed in air at various energies. Fig 4.1 shows the RBS spectra taken after laser annealing. It can be seen from the decrease in height and increase in width of the Ni signal that as the laser energy increased more of the Si substrate was melted and then interdiffused with the Ni. This resulted in a surface layer whose average Si concentration, [Si], was proportional to the laser energy. The ratio of Ni to Si present in the surface layer of a compound Ni_mSi_n can be determined from the RBS spectrum by the following equation [13]

$$\frac{m}{n} = \frac{A_{Ni}^{Ni_mSi_n}}{A_{Si}^{Ni_mSi_n}} \left(\frac{Z_{Si}}{Z_{Ni}}\right)^2 \tag{4.1}$$

where Z_x is the atomic number of element x and $A_{Ni}^{Ni_mSi_n}(A_{Si}^{Ni_mSi_n})$ is the total number of counts under the Ni (Si) signal that originate from scattering events in the Ni_mSi_n layer.

After annealing at 0.42 J[1] a significant drop (from the virgin) in the height of the Ni signal is observed, indicating that at this energy the melt front has penetrated the substrate and the liquid Ni and Si have interdiffused. Even if neither material melts there will still be some interdiffusion in the solid state due to the raised temperature. However, due to the

[1] In order to obtain the energy density it is necessary to multiply the laser output energy by a factor of 1.77 i.e. J cm^{-2} = J×1.77. Thus 0.42J is equivalent to 0.74 J cm^{-2}.

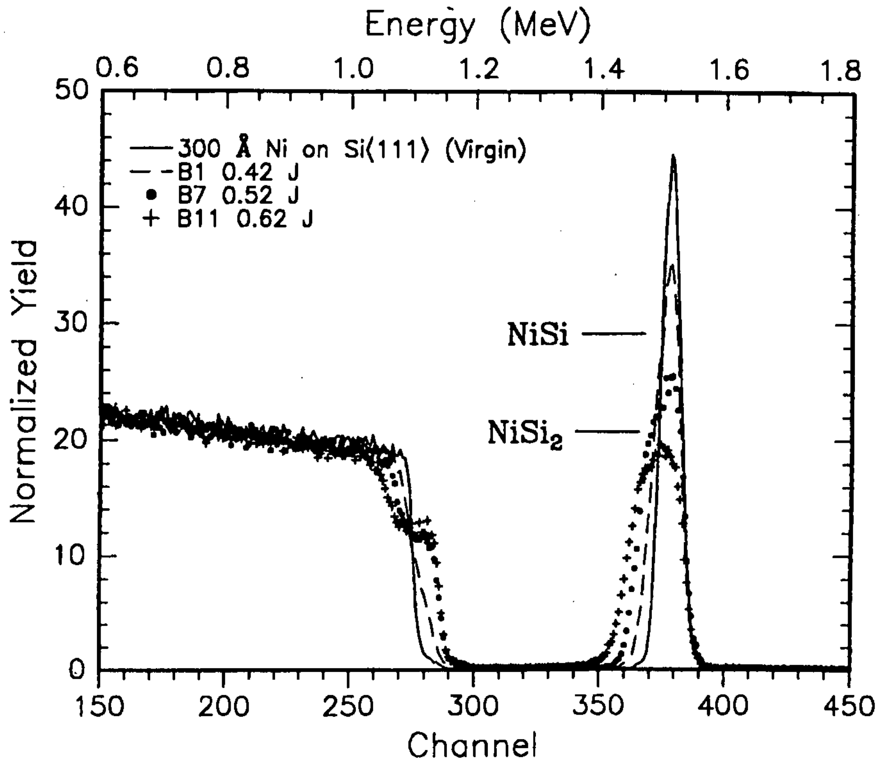

Figure 4.1: *RBS spectra of a Virgin Ni sample and after annealing at various laser energies. Note that 0.42 J is equivalent to 0.74 J* cm^{-2}. *The expected heights of the Ni signal of NiSi and* $NiSi_2$ *are also shown.*

short times spent at these elevated temperatures and the *very* big difference in solid and liquid diffusivities this effect will be small and can be ignored. It is thus estimated that a laser energy of 0.38–0.40 J is necessary for the melt front to "just" penetrate the silicon substrate. In the range 0.40–0.60 J the surface layer had a resultant silicon concentration up to about 60%. At a laser energy of 0.62 J the Ni:Si concentration ratio was found by equation (4.1) to be 1:2.1±0.1; which is more Si rich than $NiSi_2$. The error in the concentration ratio arises due to the uncertainty in estimating the silicon-substrate interface position under the total Si RBS signal.

Figure 4.2 shows the channeling spectra of two samples of different post anneal composition. The sample annealed at 0.42J (B1) has a [Ni]>50% and χ_{min}=55%; while annealing at 0.52J (B7) produced a layer with 33%<[Ni]<50% and a corresponding χ_{min}=12%. Since the [Ni] of B7 is between that of NiSi and $NiSi_2$ *and* of all the possible nickel silicides only $NiSi_2$ is known to be epitaxial on silicon; it can be postulated that annealing at 0.52J resulted in

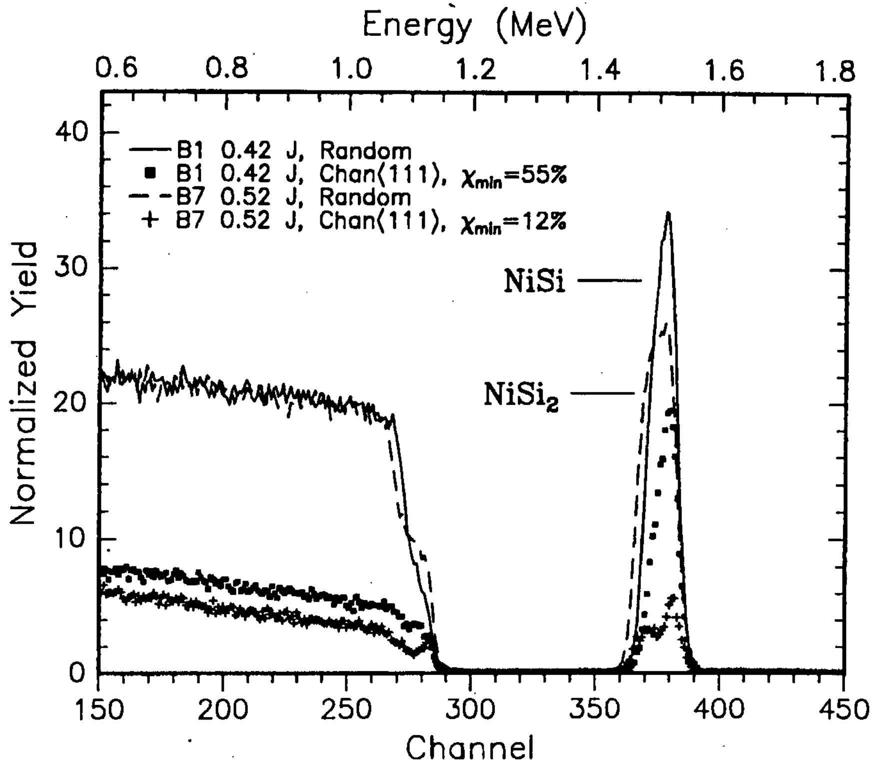

Figure 4.2: *RBS and channeling spectra at two different laser energies. Sample B7 illustrates the best χ_{min} achieved after laser annealing a 300Å Ni layer.*

the formation of grains of NiSi and $NiSi_2$. The (channeling) Ni signal of B7 shows an unusually large surface peak, indicating that the silicide layer has greater disorder closest to the surface or equivalently greater order near the substrate. For sample B1 with [Ni]>50% the channeling spectrum is very unsymmetrical; having low χ_{min} closer to the substrate and a χ_{min} ~100% in the surface layer. This could imply the existence of epitaxial $NiSi_2$ grains adjacent to the substrate and grains of NiSi and/or other metal rich phases as well as unreacted Ni closer to the surface. The best χ_{min} achieved for a 300Å Ni layer was the 12% indicated in Fig 4.2. Higher minimum yields were obtained for thicker initial layers, with χ_{min} for the 900Å samples being greatest. The back edge of the Ni signal of these thicker layers showed a slowly varying, and not steplike as in Fig 4.1, metal concentration as a function of depth — thus representing a diffusion profile. This indicates that for the thicker films diffusion (during the liquid phase) is incomplete and limited by the melt lifetime, whereas diffusion is complete for the thin layers and the final concentration is determined by the melt depth.

After the laser anneal the samples were subjected to a thermal anneal at 850°C for 30

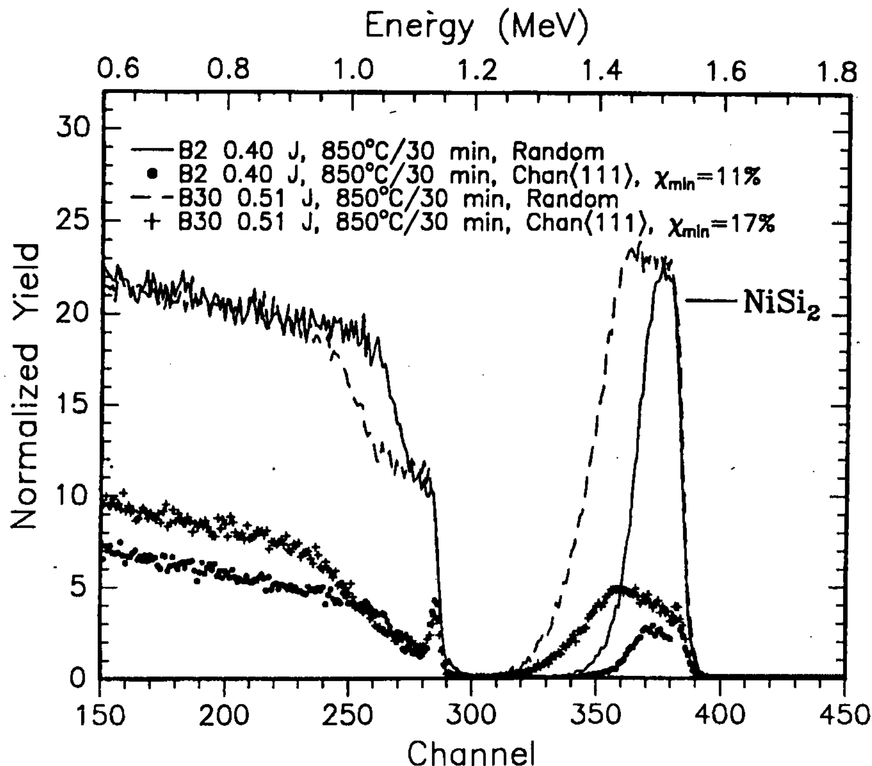

Figure 4.3: *Samples B2 and B30 show the best minimum yields achieved for 300Å and 600Å initial layers of Ni. Note the worsened interface structure.*

min. The RBS and channeling spectra of a 300Å and 600Å sample are shown in Fig 4.3. It is interesting to note that the best χ_{min} after the laser anneal did not result in the best χ_{min} after the thermal anneal. The final χ_{min} (i.e. after thermal annealing) of sample B7 actually increased to 18%. The best final χ_{min}, for all thicknesses, was achieved for samples annealed at energies just sufficient to melt through the substrate and thus produce only a small amount of interdiffusion. In these cases the laser probably produced a thin epitaxial $NiSi_2$ layer adjacent to the substrate which then acted as a seed for further solid state epitaxial growth during the thermal anneal.

The two most noticeable changes brought about by the thermal anneal, excluding the change in χ_{min}, are the *increase* in silicon disorder near the surface i.e a larger than normal surface peak and a worsening/roughening of the silicide-silicon interface. One explanation for the increased disorder in surface Si is that backscattering is taking place from a disorderd SiO_2 layer possibly formed during thermal annealing (but vacuum is $\sim 10^{-7}$ Torr). However, it is well known that the surface of $NiSi_2$ is terminated by an epitaxial Si layer 3–5 Å thick

[43] because of the lower surface energy of Si (only 52% of that of $NiSi_2$). This Si layer could have reacted with oxygen from the air and formed a thin SiO_2 surface layer. This non-epitaxial layer would cause some dechanneling and result in a "larger than pure" $NiSi_2$ silicon surface peak. The interface roughening seen in Fig 4.3, which was observed in all samples irrespective of laser energy, seems to contradict the fact that $NiSi_2$ grown thermally on Si<111> has a macroscopically perfect interface [44]. An analogy is not strictly valid since in a thermal anneal all the Ni is consumed to form the first phase Ni_2Si initially and subsequent phases are formed similarly; but a laser anneal produces $NiSi_2$ at the interface immediately. However, Ni is the diffusing species in the formation of the final phase i.e. $NiSi_2$ [45] and thus the Ni atoms diffuse through the $NiSi_2$ and then react with Si atoms at the "underside" of the $NiSi_2$ layer. If the laser annealing process then produces a silicide layer with [Ni]>33%, it can be expected that during the thermal anneal these excess Ni atoms would diffuse through the disilicide layer and react with Si atoms in the substrate. A smooth interface should thus be produced by this process as well. The following mechanism is proposed in order to explain the interface roughening.

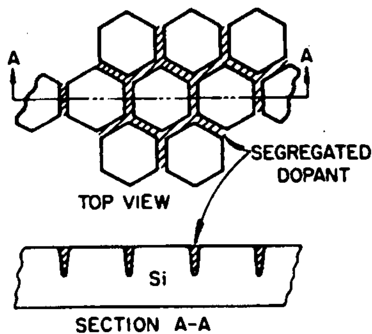

Figure 4.4: *Schematic of the resulting microstructure caused by constitutional supercooling during solidification.*

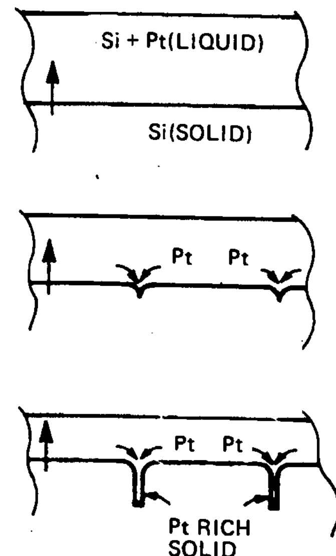

Figure 4.5: *Constitutional supercooling during regrowth of Pt in Si from the liquid phase.*

It has often been reported [46] that laser annealing of ion implanted silicon leads to

the formation of a cellular structure as shown in Fig 4.4. A similar effect is observed for the annealing of metal layers on Si substrates, but now the cells/silicon "fingers" ($\sim$ 1000Å diameter) are surrounded by walls of silicide [47]. These observations have been explained in terms of the Mullins-Sekerka theory of constitutional supercooling. If there are statistical fluctuations in the concentration of the metal across the planar melt front, the regions of greatest metal/dopant conc. will remain liquid the longest due to the depressed solidification temperature. As the melt front continues to move forward metal/dopant atoms are segregated at the interface and then swept "sideways" into nearby regions that are still liquid (see Fig 4.5). If the *depth* concentration gradient exceeds some critical value the melt front becomes unstable in terms of the Mullins-Sekerka theory and then the pure Si "fingers" protrude right through to the surface. If it is now accepted that laser annealing of the Ni layer produces such structures (as in Fig 4.6) the interface roughening may be explained. Unfortunately, no cross-sectional TEM experiments were performed and thus the existence of such structures cannot be directly verified. However, there is sufficient evidence in the literature to make this assumption at least plausible. This would imply that the silicide columns are actually more *Ni* rich than the RBS spectra in Fig 4.2 indicate (if a uniform silicide layer is assumed as above). Since the silicide columns are initiated by random fluctuations in the (lateral) metal concentration at the same depth, the final density of metal atoms in any two silicide columns is *not* necessarily equal. Now, during the thermal anneal some of the Ni atoms will nucleate to form $NiSi_2$ with all the available Si atoms within the silicide columns, and the remainder will then diffuse "outwards" and "downwards" (Fig 4.7). Thus each silicide column grows laterally and in depth; but since the Ni concentration is not necessarily the same for all columns, each column grows to a different depth (Fig 4.8). Thus the silicide-substrate interface is microscopically smooth for each column; but over a large area (as seen by RBS) the interface is rough.

Similar behaviour has been observed for Co layers on Si substrates [48]. Generally, it is thus not possible to grow single crystal epitaxial silicides from an initial metal layer by pulsed laser annealing. However, despite these difficulties Grimaldi *et al* [49] and Comrie and Hoffman [50] were able to grow epitaxial Ni and Co silicides respectively.

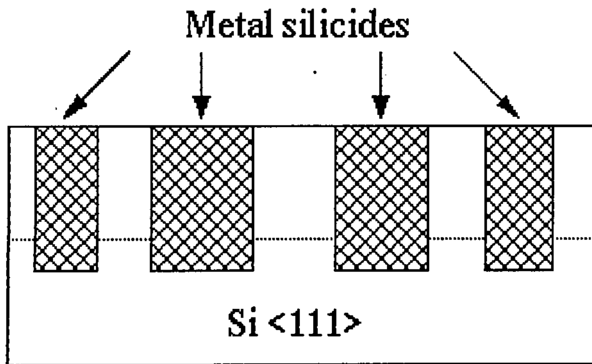

Figure 4.6: *Silicide "columns" produced by laser annealing of a pure metal layer (broken line indicates initial metal thickness).*

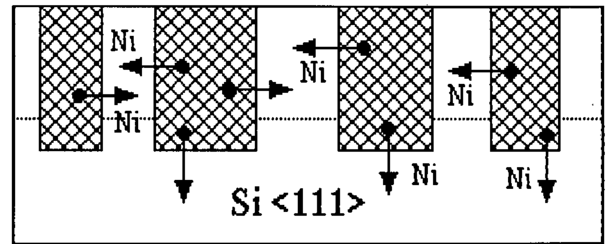

Figure 4.7: *During the thermal anneal Ni atoms diffuse "outwards" and "downwards" to form $NiSi_2$. Once individual columns have coalesced laterally excess Ni will move downwards.*

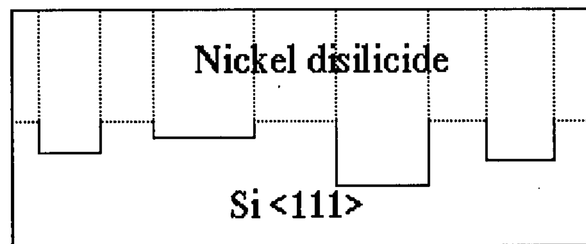

Figure 4.8: *A rough interfaced disilicide layer is produced (broken lines indicate original boundaries of silicide columns).*

4.2 Monosilicides on Silicon ⊲111⊳ and ⊲100⊳ substrates

In order to avoid constitutional supercooling effects it was decided to first thermally grow a silicide and then perform the laser annealing. This would decrease the concentration gradient "seen" by the moving liquid-solid interface and thereby force the interface to remain stable [2]. It was, however, discovered by Tung *et al* [51] that better epitaxy can be achieved if the starting compound is the monosilicide and not the disilicide. The approach of Tung *et al*

[2]Analysis of equation (20) in W.W Mullins, R.F. Sekerka; *J. Appl. Phys.*, **35**, 444 (1964) shows under what conditions instability of the interface can be expected. This also provides an estimate of the cell size if the instability is "weak" i.e. a small perturbation.

was followed in this work.

Since the thinnest layers gave the best epitaxy above it was decided to use only 300 Å metal layers for the rest of this study. Nickel and cobalt layers of 300 Å thickness were deposited onto chemically cleaned Si <111> and <100> wafers. These samples were then removed from the evaporation chamber (thus exposed to the atmosphere) and some annealed for 30 min at 550°C and 750°C to form $CoSi_2$ and $NiSi_2$ respectively. The rest of the samples were annealed at 450°C and 650°C to form CoSi and NiSi. These samples were laser annealed at various energies and then subjected to a further thermal anneal.

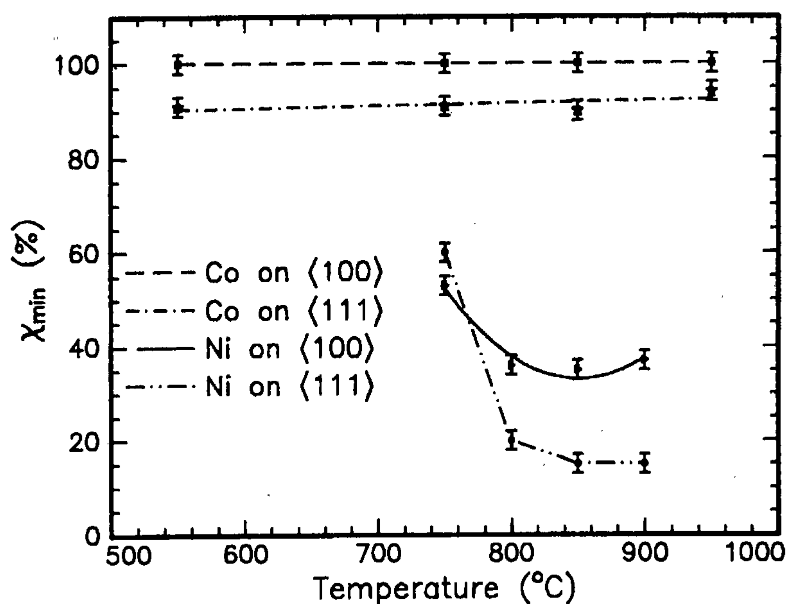

Figure 4.9: *Minimum yield after furnace annealing at various temperatures.*

The minimum yields measured after the formation of Ni- or $CoSi_2$ by the pure thermal anneal are shown in Fig 4.9. The results for Ni span a much narrower temperature range due to the higher formation temperature of $NiSi_2$ (750°C as opposed to 550°C for $CoSi_2$) and the "depth" of the liquidus minimum in the Ni-Si phase diagram. The Ni-Si liquidus minimum occurs at about 940°C. It can be seen that the χ_{min}'s for both substrate orientations are significantly better in the case of Ni; while the minimum yield for a <111> substrate is consistently lower than that for a <100> substrate. The only exception to this general trend is Ni at the formation temperature, but this difference is only $\sim$ 5%. It is well known that thermal annealing of (Ni and Co)/Si thin film diffusion couples leads first to the growth of

metal-rich silicides (Ni_2Si and Co_2Si) followed by the monosilicides (NiSi and CoSi), and eventually the disilicides ($NiSi_2$ and $CoSi_2$). Marker experiments show that the metal is the dominant diffusing species in the growth of Ni_2Si, Co_2Si and NiSi, while diffusion of Si dominates in the formation of CoSi [52]. Metal is the diffusing species in the formation of both $CoSi_2$ [52] and $NiSi_2$ [53]. The formation of $NiSi_2$ is nucleation controlled and growth is upwards in thin columns and then radially outwards [54]. Nucleation plays a less important role in $CoSi_2$ formation because the kinetics are complex (i.e. a superposition of several mechanisms: diffusion, nucleation and interface reaction) [52].

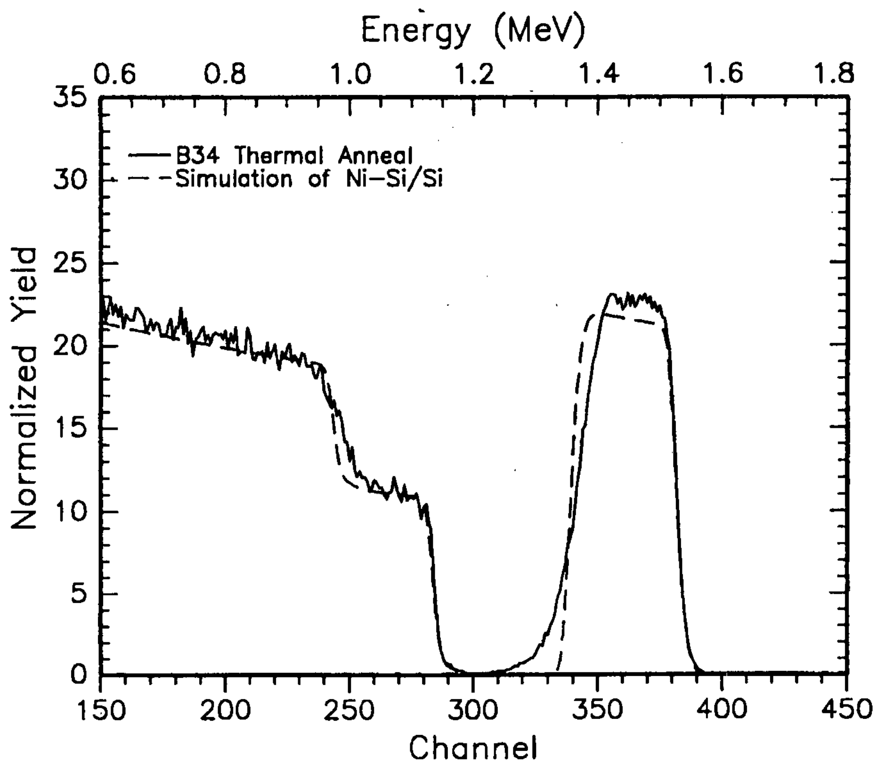

Figure 4.10: *RBS spectrum for thermally grown $NiSi_2$ on a <100> substrate. A theoretical spectrum is overlayed to illustrate the badly defined interface.*

From Fig 4.9 it is seen that the easiest system for epitaxial growth is Ni on <111>. These thermally grown $NiSi_2$ layers contain mixed A and B orientations, with Type B occupying slightly more than 50% of the film [44]. Type A $NiSi_2$ (and $CoSi_2$) has the same orientation as the silicon substrate while Type B shares the surface normal <111> axis with the Si substrate but is rotated 180° about this axis with respect to the Si. Thermal growth of $NiSi_2$ from a Ni layer on Si <100> also leads to fair (~40%) epitaxy but layers grown in this manner are very non-uniform in thickness, as demonstrated by Chiu *et al* [44]. This bad

interface is shown in Fig 4.10 and is seen from the trailing low energy edge of the Ni signal. This bad interface is due to faceting of the original interface along {111} planes. These facets are approximately ~750Å in length. The minimum yields for Co on <111> substrates were surprisingly high; a yield at least lower than 90% could be expected simply in view of the small lattice mismatch and similar crystal structures. This result is in contradiction with reference [50] where a χ_{min} of 60% was found. It was also a general finding during the course of this investigation that cobalt was much more susceptible to the vacuum condition and surface cleanliness than nickel. The cobalt used in this investigation was only 99.9% pure; while that used in [50] was zone refined and thus much purer. This high level of impurities could have contributed to the increased minimum yield. No measurable degree of channeling was found for Co on <100> substrates. Unlike $NiSi_2$ epitaxy on Si <100>, faceting does not occur for epitaxial $CoSi_2$ on <100>. Instead, the biggest stumbling block is multicrystallinity [55]. There are numerous competing orientations for $CoSi_2$ epitaxy on Si <100>; normal A type, also a twinned B Type, those related by a 90° rotation ($CoSi_2(110) \| Si(100)$) and even one where the $(22\bar{1})$ plane of $CoSi_2$ is parallel to the (100) plane of Si. Despite these difficulties it has been shown that $CoSi_2$ can be grown epitaxially on Si <100> by means of a TiN interlayer [56]. This method gives a minimum yield of about 18%.

The results of channeling measurements on samples which went through the sequence 1) thermal anneal to form a monosilicide 2) laser anneal and 3) final thermal anneal, are shown in Figures 4.11 and 4.12. The final anneal was performed at two different temperatures, i.e. 700°C and 950°C for Co and 800°C and 900°C for Ni samples. On average it is seen that Ni on <111> gives the best minimum yields. χ_{min}'s as low as 18% were measured immediately after the laser anneal. In all cases it is seen that the highest yields are obtained after laser annealing while the lowest yields occur after the highest temperature anneal. This general trend can be explained by noting that due to the very high quench rates (of the order of 10^{10} Ks^{-1}) involved in the laser annealing process; the silicides so formed will be highly defective. The final anneal then allows the crystal structure to relax and also provides the means for any necessary diffusion of Ni (Co) atoms to form a complete layer of $NiSi_2$ ($CoSi_2$). However, perfectly relaxed epitaxial silicides cannot be expected at room temperature due to the difference in lattice constants[3] and thermal conductivities[4]. A simple calculation shows

[3] a_o = 5.431, 5.407 and 5.379 Å for Si, $NiSi_2$ and $CoSi_2$ respectively

[4] Thermal conductivities are (3; 16 and 12)$\times 10^{-6}$ K^{-1} for Si, $NiSi_2$ and $CoSi_2$ respectively.

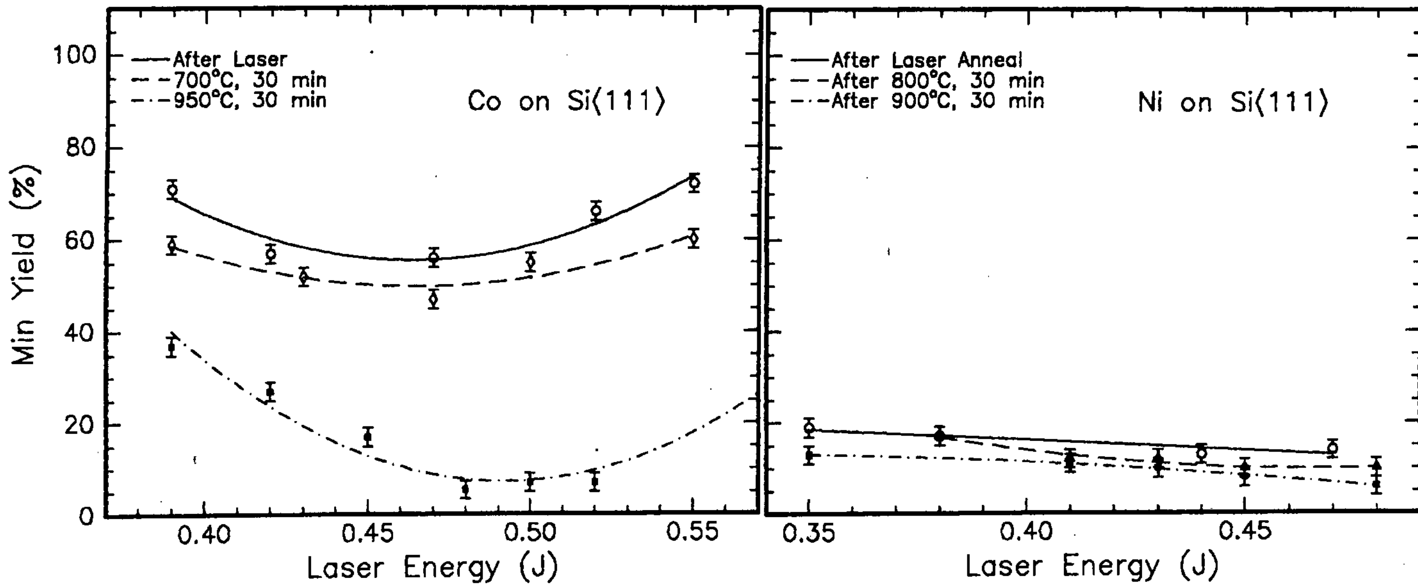

Figure 4.11: *Minimum yield as a function of annealing energy for NiSi and CoSi starting layers on <111> substrates.*

zero lattice mismatch between $NiSi_2$ and Si at $\sim$ 380°C and, for the $CoSi_2$-Si system, at $\sim$ 1100°C. Hamm *et al* [57] have shown that the lattice mismatch is different for A and B type ($NiSi_2$) and also a function of the angle from the surface normal. This difference in A and B Type lattice constants and the anisotropy of the supposedly cubic structure of $NiSi_2$ will cause stress effects that thermal annealing would not be able to eliminate totally. It is thought that this effect would be greater in $CoSi_2$ (due to the larger lattice mismatch) and thus could be one of the factors resulting in higher χ_{min}'s for Co samples. From Fig 4.12 it is seen that the worst minimum yields are obtained for Co on <100> substrates. χ_{min}'s only as low as 35% could be achieved, which is similar to that obtained by UHV deposition and reaction. The cobalt sample χ_{min} after the lower temperature final anneal exhibit a tendency to increase at higher laser energies (especially on <100> substrates). This is probably due to the presence of impurities.

Figure 4.13 shows two RBS spectra taken after the final anneal (at 800°C for 30 min) of a Ni on <100> sample. One spectrum was taken inside the laser spot while the second was taken outside the spot i.e. an area subjected to two successive thermal anneals — 650°C for 30 min and 800°C for the same time. It can clearly be seen that the laser formed

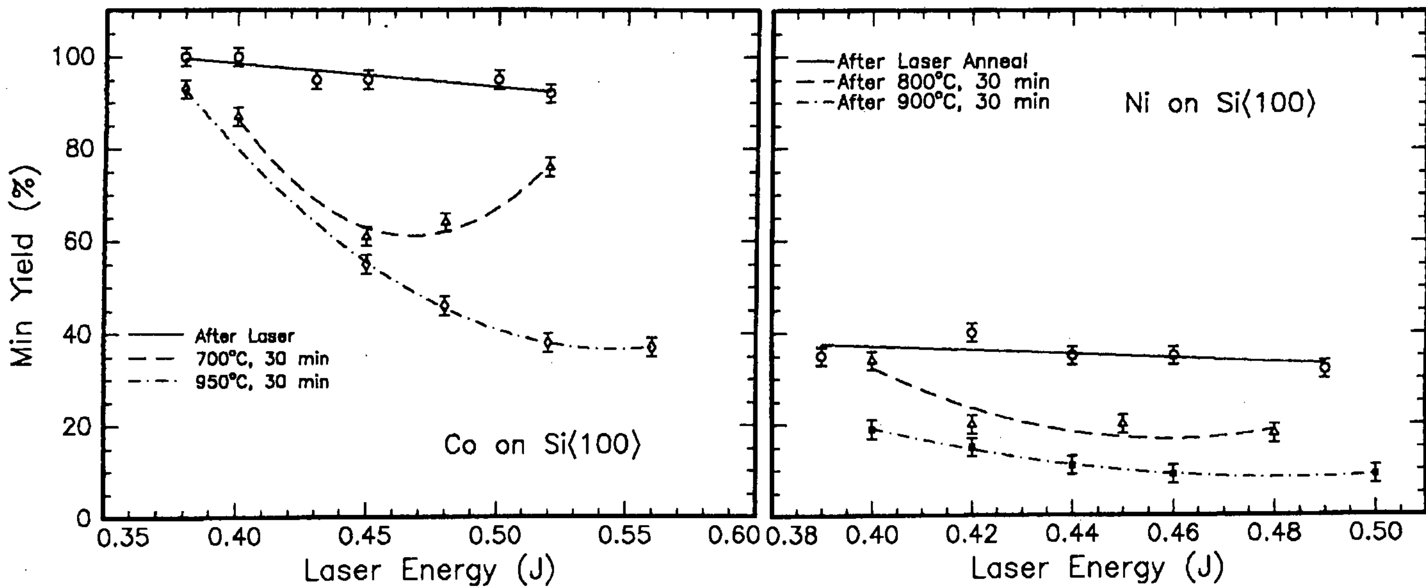

Figure 4.12: *Minimum yields as a function of annealing energy for NiSi and CoSi starting layers on* <100> *substrates.*

disilicide has a perfect interface while the interface in the thermally grown region is worse — indicative of faceting along {111} planes as explained above. This illustrates that the $NiSi_2$/Si<100> interface *is* stable, contrary to the argument given by Lau and Cheung [54] in order to explain the interface breakup. Before the laser anneal the NiSi/Si interface is seen by RBS to be smooth. Thus the laser annealing and subsequent rapid quench preserves this interface structure.

The RBS and channeling (down the <111> axis) spectra of $NiSi_2$ on a <111> substrate are shown in Fig 4.14. This illustrated the lowest minimum yield (5%) measured for $NiSi_2$ on a <111> substrate. Similar levels of epitaxy were detected for $CoSi_2$/Si<111> while slightly higher best χ_{min}'s were found for $NiSi_2$/Si<100>. Figure 4.15 shows channeling spectra taken the <110> and <114> axes of the substrate for the same sample as in Fig 4.14. A random spectrum taken 2 degrees away from the <110> position is also shown in Fig 4.15. From the insert in Fig 4.15 it can be seen that in the case of a cubic structure the <114> and the <110> directions have the same polar angle from the <111> surface normal. The <110> and <114> axes were found by rotating the sample through 35.3° from the <111> channeling position and then rotating through 360° around the <111> axis.

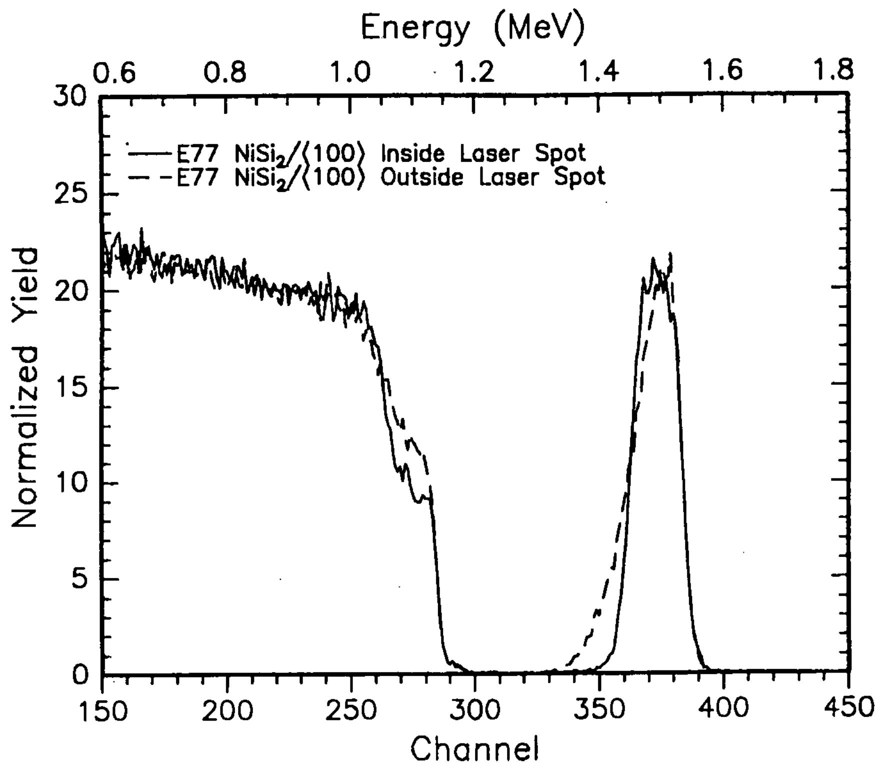

Figure 4.13: *RBS spectra taken inside and outside the laser spot. The laser formed* $NiSi_2$ *exhibits very good interface "structure".*

Six dips in backscattering yield are then observed and these correspond to alternate <110> and <114> directions. Theoretically it is expected that the yield down a <110> direction (corresponding to scattering from (110) planes) be lower than that down the <114> direction (scattering from more densely packed planes) and that the ratio χ_{min}<114>/χ_{min}<110> = 2.4 [13]. In Fig 4.15 it is seen that the minimum yields "cross over" at the interface i.e. the larger yield in the substrate becomes the smaller yield in the silicide and vice versa. This implies that when channeling down the <110> axis of the substrate, channeling down the <114> axis of the silicide is taking place simultaneously. A similar argument applies to the <114> substrate direction. This in turn implies that the surface layer must be opposite in orientation to the substrate i.e. Type B. However, the ratio of minimum yields in the Ni signal is only 2.15 and not 2.4 as expected. This "disagreement" could be due to lack of perfect epitaxial $NiSi_2$ and/or a mixture of Type A and Type B orientations in the silicide. Thus the larger χ_{min} in the Ni signal (corresponding to channeling down the <110> in the substrate) is actually due to channeling down the <110> directions of A Type crystals plus channeling down the <114> direction of B Type crystals. If one assumes that the silicide is

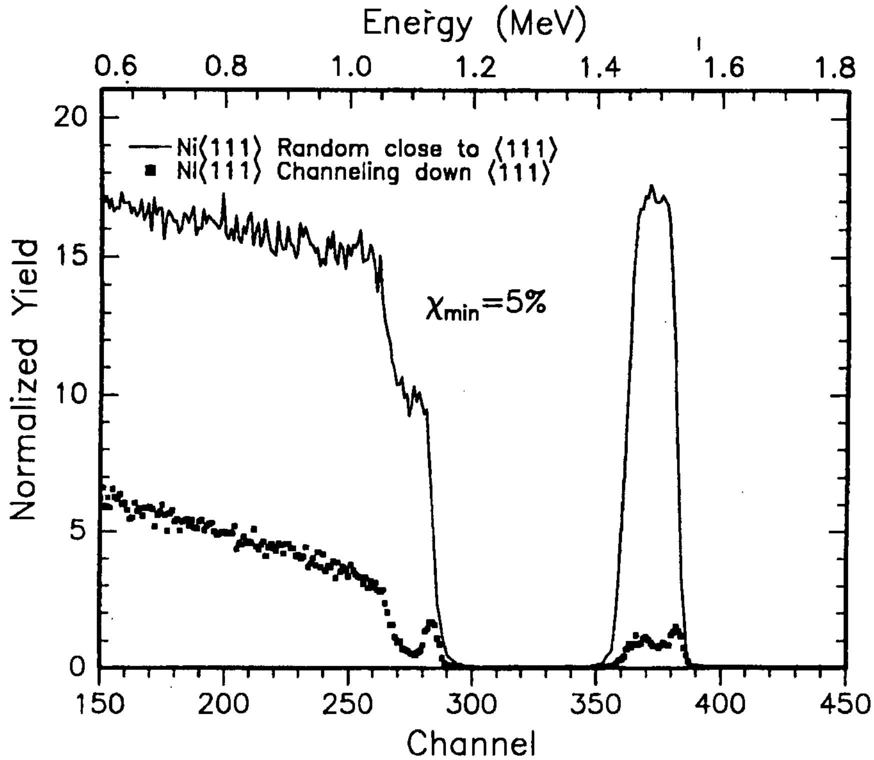

Figure 4.14: *Random and aligned spectrum of NiSi₂/Si<111>.*

made up of a% A Type and b% B Type then the following expression is proposed to describe the observed ratio of yields in the Ni signal

$$\frac{\chi_{min}(larger)}{\chi_{min}(smaller)} = \frac{b\ \chi_{min} <114> +a\ \chi_{min} <110>}{a\ \chi_{min} <114> +b\ \chi_{min} <110>} \tag{4.2}$$

where the LHS is the measured ratio (i.e. 2.15). This expression can be rewritten as

$$\frac{\chi_{min} <114>}{\chi_{min} <110>} = \frac{2.15b - a}{b - 2.15a}. \tag{4.3}$$

If the LHS is now replaced by the theoretical value of 2.4 and it is noted that $a + b = 100$, it is found that $a = 5.6$ and $b = 94.4$. Thus the silicide layer is made up of 94% B Type and only 6% B Type. Similar values were found in reference [50] for the case of $CoSi_2$. However, it was found by Tung *et al* [51] that when channeling yields indicated the silicide was 95% B Type; TEM showed that there was actually no A Type present at all i.e. the silicide is 100% B Type. On several occasions after the final anneal it was noticed that the laser spot was still shiny/silver while the surrounding areas were already darker, characteristic of the disilicide phase. This was more readily observed in the case of Co because of the bluish

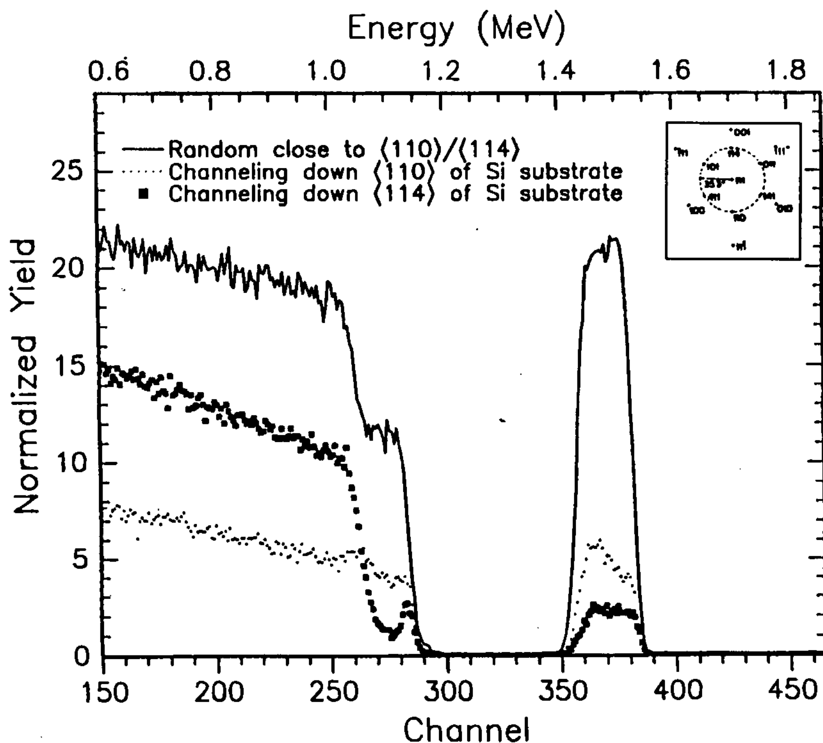

Figure 4.15: *Random and channeling spectra measured down the <110> and <114> directions.*

colour of $CoSi_2$. Since the outer regions are known to be of mixed A and B Type and the laser irradiated area is (almost) only B Type; this observation could be an indication that grains of B Type material have not yet nucleated in the laser spot or if these grains have nucleated that they have not yet grown to the surface. This is in line with the observations that B Type material grows about 10 times slower than A Type material [58].

The <111> wafers used in this investigation were miscut by 4°. This would cause the surface to become a series of "true" (111) planes separated by steps. If the step height is assumed to be one layer (i.e. 3.14Å) then the ledges are about 40Å in length (see Fig 4.16). Since it is assumed that the melt front moves perpendicular to the (macroscopic) surface normal at all times; the regrowth velocity is then faster than it would be in the <111> direction (see section 3.3.2). It is known that very high regrowth velocities lead to amorphous materials but the increase in velocity due to a 4° tilt should be marginal. The presence of steps will, however, provide favourable nucleation sites for growth from the melt since attachment of atoms at a ledge site leads to fewer broken bonds than attachment to an atomically flat surface. It has been shown through X-ray rocking curve measurements that

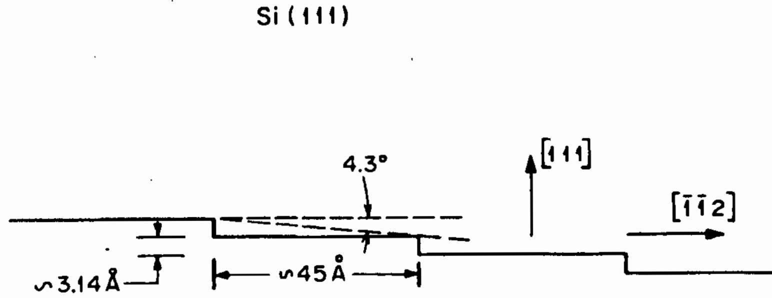

Figure 4.16: *Schematic illustration of the surface of a <111> wafer miscut by 4.3°.*

the <111> direction of an epitaxial $CoSi_2$ layer grown on a miscut wafer is neither parallel to the substrate <111> direction nor the surface normal [59]. The silicide <111> direction is found to lie between these two extremes i.e. $0^o < \text{<111>}_{silicide} < 4^o$. The misorientation between silicide and substrate $< 111 >$ directions is thus about 2°. This misorientation introduces additional strain at the interface and therefore could lead to an increased density of defects. These defects along with the misorientation would lead to dechanneling at the interface and may be partly responsible for the sometimes observed increase in χ_{min} close to the interface.

Figures D.1 - D.4 show SEM micrographs [5] of Ni-Si<111>, Ni-Si<100>, Co-Si<100> and Co-Si< 111 > systems respectively. These micrographs are presented in Appendix D for convenience. For each of these systems only the samples showing the best degree of *final* epitaxy were examined. The left hand side of each of these figures shows a region within the laser spot while the right hand figure shows a random region outside the laser spot. It should be noted that these figures do not allow comparison between laser assisted epitaxial layers and those grown from a *single* thermal anneal since the outer regions of the examined samples were subjected to *two* thermal anneals, the first of which being used to produce a monosilicide. Figure D.1 shows two backscattered electron images while secondary and backscattered images are shown from Fig D.2 onwards. Each of these latter images is split with the backscattered image being on the right. Since the backscattered images were

[5] Strictly these are not the original micrographs, or even Xerox copies thereof but rather black and white digital reproductions. Unfortunately some resolution has been lost in this reproduction but the images are still good enough to allow comparison.

recorded in compositional and not topographical mode, the contrast within the image arises due to differences in atomic number. The lighter regions thus correspond to areas of higher metal concentration. The backscattered image also provides information from greater depths than the secondary electron image.

From Fig D.1 it is immediately obvious that the laser has produced a region that is much more uniform than the thermally grown area. This is the case in all four systems, although there is little difference in the case of Co-Si<111>. The secondary electron images show the surfaces, both inside and outside the laser spot, to be mostly characterless — with Co-Si<100> being the smoothest. The regions outside the laser spot of Co-Si<100> show large concentrations of metal ($\sim 1\mu$m) surrounding large "pinholes" ($\sim \frac{1}{2}\mu$m). At higher magnification it is seen that these "pinholes" penetrate through to the substrate. Similar "pinhole" structures are observed for the other systems but in none of these is the metal concentration gradient as steep. Due to time constraints no secondary electron images were recorded for a glancing incident angle (i.e. not 90°) and thus no vast topographical differences were recorded. It has, however, been suggested that the growth within the laser irradiated area is in a layer-by-layer fashion in contrast to the (mainly) nucleation controlled growth of the outer regions [60].

Figures D.5 and D.6 show secondary electron images of CoSi and NiSi after annealing at high energies. Annealing at these energies (0.62 J on 1100 Å of monosilicide) produces a layer with [Ni] much less than 33%. The "CoSi" is severely damaged while the "NiSi" has survived intact. The damage to the cobalt layer is clearly visible to the naked eye. The fractures are seen to follow two very well defined directions which are separated by 60°. For this reason it is thought that the fractures are parallel to the $<11\bar{2}>$ and $<\bar{1}2\bar{1}>$ directions.

4.3 Epitaxial Monosilicides

During the course of this investigation it was noticed that after thermally growing NiSi and laser annealing at an energy just sufficient to melt through to the substrate that a large reduction in channeling yield was obtained. The thermally grown NiSi exhibited no channeling at all (i.e. $\chi_{min} = 100\%$) but after the laser anneal the minimum yield was $\sim$35%. The RBS and channeling spectra of such a sample are shown in Fig 4.17. This shows

that the [Ni] is very close to 50% (compare to theoretical spectrum) and thus the silicide is macroscopically still NiSi. With such a large deviation from $NiSi_2$ structure it cannot be postulated that the silicide is partly $NiSi_2$. If this were the case then it would be necessary to have the Ni rich silicides present as well; in order to bring the [Ni] up to ~50%. This also seems unlikely in view of the fact that the starting material was already NiSi. Similar results were obtained by Baeri *et al* [61] and it was concluded that the (partial) epitaxial silicide had a *cubic* symmetry with a lattice constant very close to that of Si. However, the only documented structures of NiSi [62] are an *orthorhombic* MnP structure and a cubic FeSi structure with a lattice mismatch of ~ 20% on silicon. No similar epitaxial CoSi structure was found during the course of this investigation (CoSi also has an equilibrium cubic FeSi structure and lattice mismatch of ~ 20% on silicon). However, there have been reports [63] of an epitaxial CoSi structure but this was observed during MBE formation of $CoSi_2$.

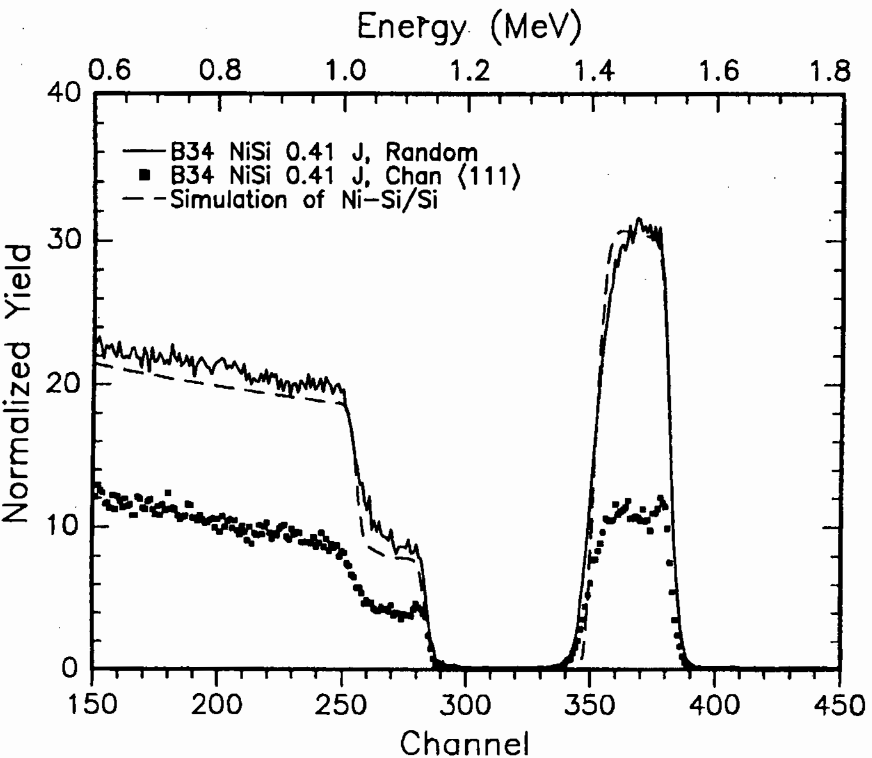

Figure 4.17: *Channeling spectrum showing epitaxial (35%) NiSi.*

It is thus suggested that upon recrystallisation either the silicide takes up the epitaxial $NiSi_2$ structure but with a *large* number of vacancies; or that the NiSi crystallises into a non-equilibrium phase (not well documented). Evidence supporting the first idea are the observations of non-stoichiometric $NiSi_2$. A composition of $Ni_{1.04}Si_{1.92}$ has been deduced

from bulk crystals [55], with 1.4% Si vacancies as well as 2% antisite defects (Ni atoms on Si sites). This effectively gives a silicide of $NiSi_{1.85}$ (as would be measured by RBS). By comparison, the disilicide phase of cobalt is always found to be nearly stoichiometric [55]. The great structural similarity between CoSi and FeSi and the reported epitaxial behaviour of CoSi lends support to the latter idea proposed above [64].

It is thus postulated that NiSi takes on a non-equilibrium epitaxial structure due to the very rapid solidification induced by laser annealing. This results in a silicide that has a very high strain energy and thus decomposes/relaxes upon thermal annealing. After thermal annealing at 300°C this metastable NiSi is known to transform into the equilibrium orthorhombic structure [61].

4.4 Co/Ni bilayers on <111> and <100> substrates

Layers of Co and subsequently Ni were deposited onto <111> and <100> wafers as previously described. Two sets of samples were prepared — one set with 250 Å of Co and 50 Å of Ni, referred to here as Ni (thin) samples; and the other set of samples with 200 Å of Co and 100 Å of Ni will be referred to as Ni(thick). As before the samples were first thermally annealed to form the monosilicide but now a reaction temperature of only 400°C was required. This is considerably lower than the formation temperature of both NiSi and CoSi. Once the monosilicide is formed it is seen that the NiSi and CoSi separate into two distinct layers with NiSi always closest to the Si substrate. This remains true irrespective of the initial configuration [65]. These samples were subsequently laser annealed at various energies and finally furnace annealed at 900°C.

The best minimum yield achieved by this process on a <111> substrate was equivalent to the best achieved for both Ni and Co on <111> i.e. $\sim$ 5%. No difference was found between Ni(thin) and Ni(thick) behaviour. Figure 4.18 shows a RBS and channeling spectrum from a Ni(thick) sample. Due to the common crystal structure and almost identical lattice parameters; the disilicides, unlike the monosilicides, are mutually soluble. The laser anneal has thus probably produced a CaF_2 crystal structure with the metal lattice sites now being occupied by either Ni or Co atoms.

It was originally hoped that by producing a layer of thin NiSi underneath a CoSi over-

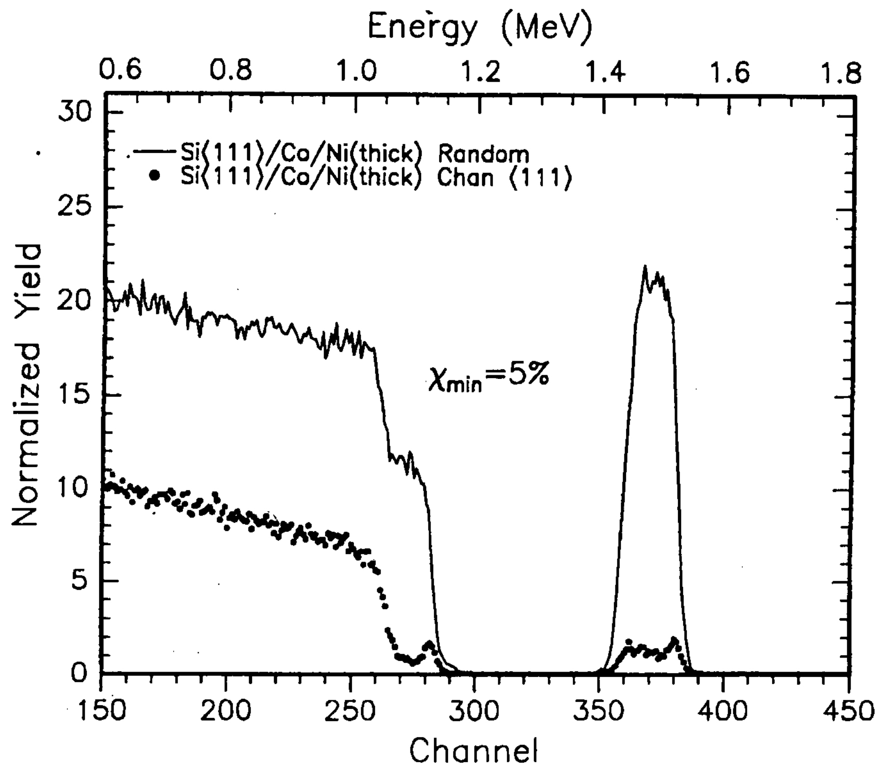

Figure 4.18: *RBS and channeling spectrum from an initial sample configuration of Si/200ÅCo/100ÅNi: Very good minimum yields are obtained.*

layer (on a <100> substrate) that the epitaxy of $CoSi_2$ on <100> could be improved. For the Ni(thin) samples i.e. 50 Å Ni, the behaviour was exactly as for pure $CoSi_2$ on <100> — lowest χ_{min}=35%. However, for the thicker Ni layers the best χ_{min} was found to be 26% (see Fig 4.19). There thus appears to be some critical Ni concentration between 17% and 33% at which the epitaxial behaviour becomes more like that of Ni on <100>.

4.5 Results of Numerical Calculations

As described in chapter 3 numerical calculations were undertaken to simulate the laser annealing of monosilicide surface layers on crystalline silicon substrates. A purely heat flow approach was adopted and no interfacial kinetics were taken into account. Thus the liquid-solid interface remained at the equilibrium melting temperature throughout. A plot of the maximum melt depth as a function of the laser energy is given in Fig 4.20 for the case of 700 Å of monosilicide (Ni and Co) on a crystalline substrate. Since a depth increment of 100 Å was chosen for all the calculations; a 700 Å surface layer most closely resembled the actual

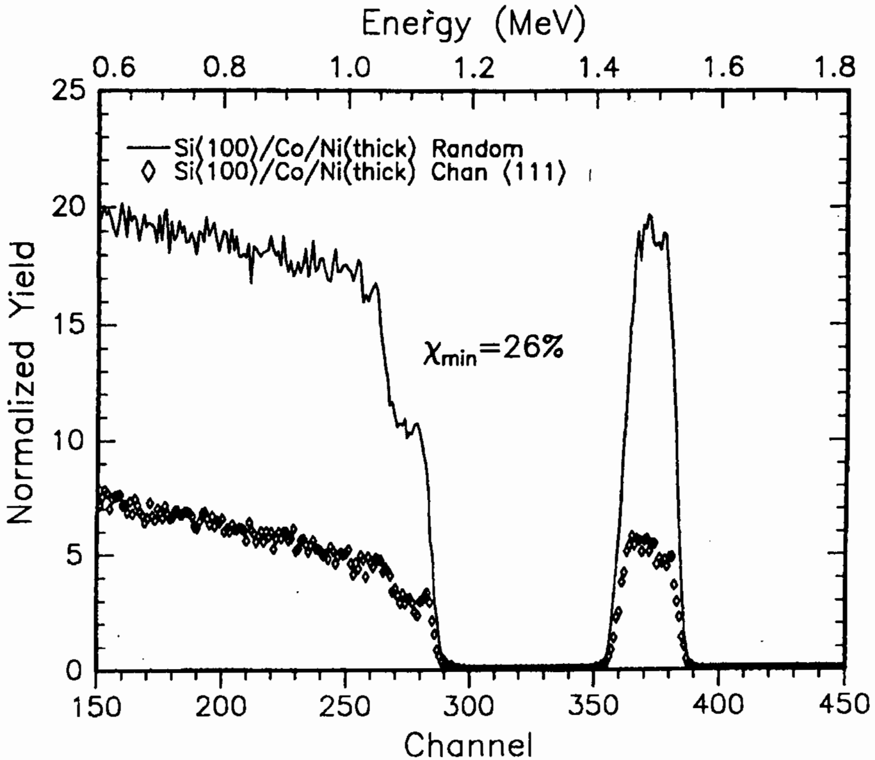

Figure 4.19: *The best minimum yield for a Ni(thick) sample. The epitaxial behaviour is now moving away from that of Co-Si*<100> *to that of Ni-Si*<100>.

structure of the sample. Figure 4.20 predicts that the surface should melt at 0.21 J and 0.28 J for NiSi and CoSi respectively. It should be noted that *energy density* is the important physical parameter and not energy *per se.* Thus NiSi melts at 0.37 J cm^{-2} and CoSi at 0.50 J cm^{-2}. This difference in melting threshold can be attributed to the large ($\sim$ 500K) difference in melting temperatures of CoSi and NiSi. For NiSi it is seen that once the silicide is completely melted there is a large energy step before any penetration into the substrate takes place. This can be attributed to the large difference in NiSi and crystalline Si melting points as well as the large heat of fusion of silicon. In contrast the CoSi curves show only a small, if any, ledge at a depth of 700 Å. For CoSi the strange phenomena of "substrate melting before complete silicide melting" can be seen. At energies which have almost melted the entire silicide layer it is seen that the upper most regions of the substrate have begun to melt (indicated by stars). This phenomenon extends over an energy range of about 0.02J before the whole silicide layer is melted. Even though the melting temperature of CoSi is slightly higher than that of Si ($\sim$ 50K); this is an unexpected occurrence, especially in view of the large heat of fusion for silicon. It is thus seen that substrate penetration occurs at

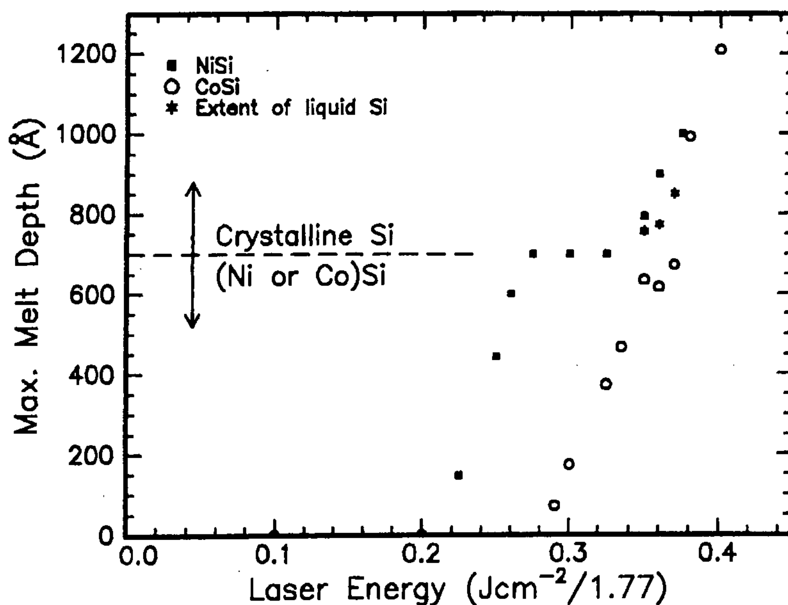

Figure 4.20: *Maximum melt depth for various incident laser pulse energies. The stars indicate the depth of the "Si melt front" in cases where the underlying substrate has melted before the silicide is 100% melted.*

about 0.34 J and 0.37 J for NiSi and CoSi respectively. From the RBS spectra substrate penetration energies were found to be 0.38 J and 0.40 J for NiSi and CoSi respectively. This discrepancy between calculated and observed substrate penetration energies is due to the weak detection limits (of the order of 10^{14} atoms cm^{-2}) of the RBS technique. In order to notice any change in the RBS spectrum after laser annealing it is necessary for the melt front to penetrate deeply enough into the substrate so that sufficient intermixing of metal and silicon atoms can occur. This would correspond to a higher laser energy than that for *just* melting into the substrate, thus narrowing the gap between calculated and measured substrate penetration energies.

Figures 4.21 and 4.22 show the temperature versus depth profiles at various times of a NiSi sample shot at 0.35 J and a CoSi sample shot at 0.37 J. In general it is seen that after short times the temperature gradients are large, which would result in undercooling of the liquid (not taken into account here). After longer times the temperature gradient, in the liquid especially, decreases. The position of the liquid-solid interface as a function of time is shown in Figures 4.23 and 4.24. Once again the large difference in NiSi and Si

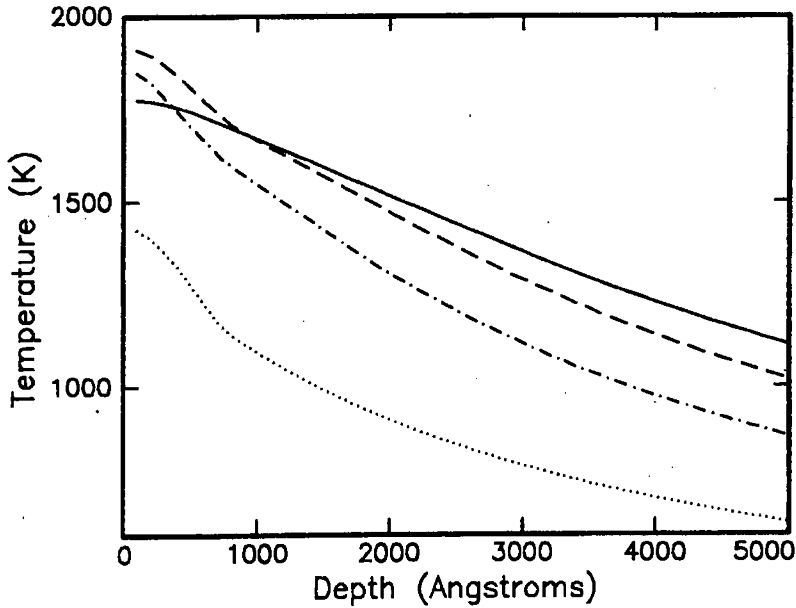

Figure 4.21: *Temperature versus depth for a CoSi sample annealed at 0.37 J. The curves are taken at different times : 40 nsec (dots); 50 nsec (line-dot); 60 nsec (broken) and 70 nsec (solid).*

melting temperatures manifests itself through large steps on the NiSi curve. The step on the "inward" part of the curve is smaller than on the "outward" part of the curve due to the larger thermal gradients present at earlier times. In comparison with Fig 3.3 it is estimated from Figures 4.23 and 4.24 that the maximum interface velocity would occur at $\sim$ 70 nsec for both NiSi and CoSi at energies that produced about 100 Å of substrate melting. In order to estimate the undercooling at the interface equations (3.16) and (3.17) will be used, i.e.,

$$\Delta T_{max} = \frac{X}{1+X} T_m \tag{4.4}$$

where

$$X = \frac{RT_m}{M\,\Delta H_{sl}} ln \left[1 - \frac{K_s}{aA\nu_i} \left(\frac{\partial T_s}{\partial z} \right)_i \frac{1}{\rho \Delta H_{sl}} \right]. \tag{4.5}$$

In order to evaluate the above expressions the following numerical values were used

- using a data analysis software package it was determined that the thermal gradients in NiSi and CoSi were -1.19$\times 10^7$ and -1.54$\times 10^7$ K cm^{-1} respectively. These are values

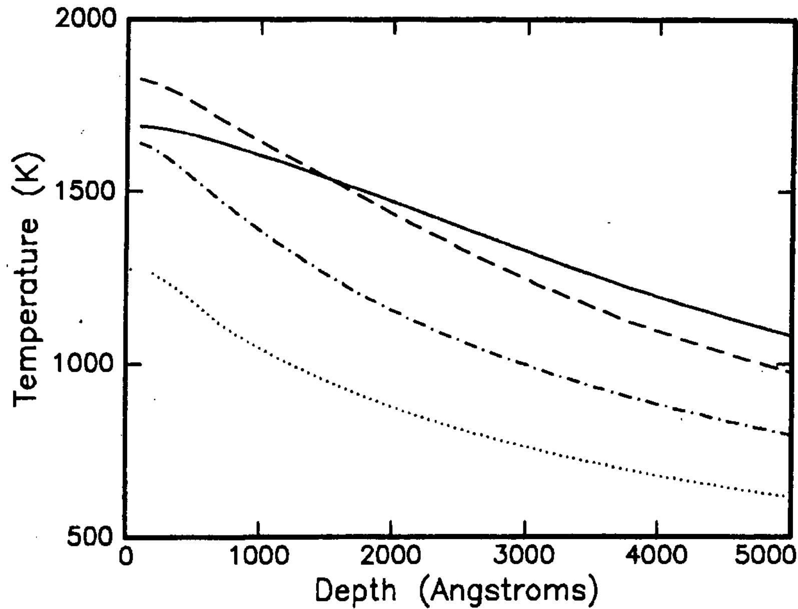

Figure 4.22: *Temperature versus depth profile for NiSi annealed at 0.35 J. Time labellings are as above.*

at 70 nsec and at a depth given by the liquid-solid interface.

- an interatomic spacing, a, of 2.5 Å for both CoSi and NiSi. Spacing between the {111} planes of NiSi is 2.51 Å while for CoSi it is 2.57 Å.

- an accommodation probability equal to 1 for both silicides. This implies that a rough interface has been assumed. In terms of Jackson's rule [38] this is not strictly correct. The value of $|\Delta H_{sl}|/T_m$ is slightly greater than 4R for both CoSi and NiSi and thus a smooth interface is predicted.

- an attachment frequency, ν_i, equal to 10^{11} $\sec^{-1}$ (see chapter 3), and

- the remaining values were taken form Appendix C.

Equation (3.16) thus predicts a maximum undercooling of $\sim$ 98K for NiSi and $\sim$ 29K for CoSi. Galvin *et al* [66] "measured" (indirectly through transient conductance techniques) a maximum undercooling of 89K for the ruby laser annealing of silicon-on-sapphire.

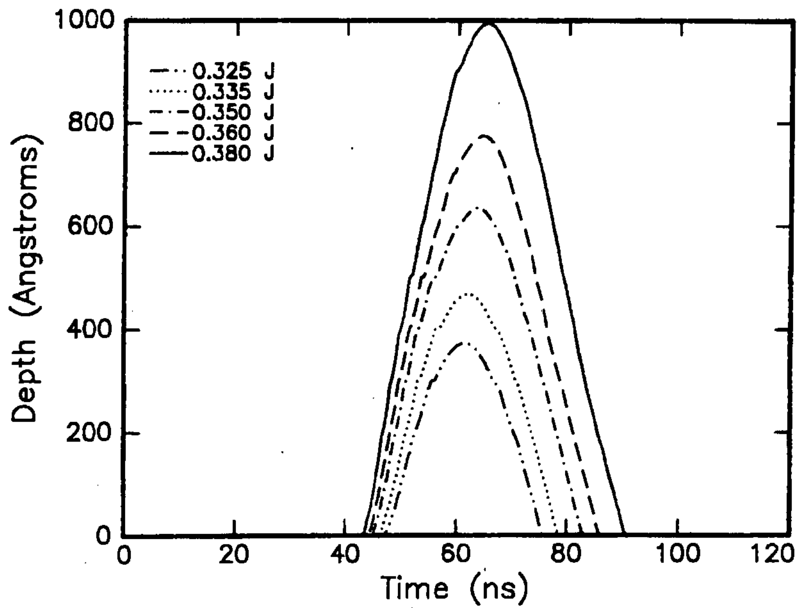

Figure 4.23: *Calculated liquid-solid interface position as a function of time for CoSi. Higher energies naturally lead to greater penetration depths.*

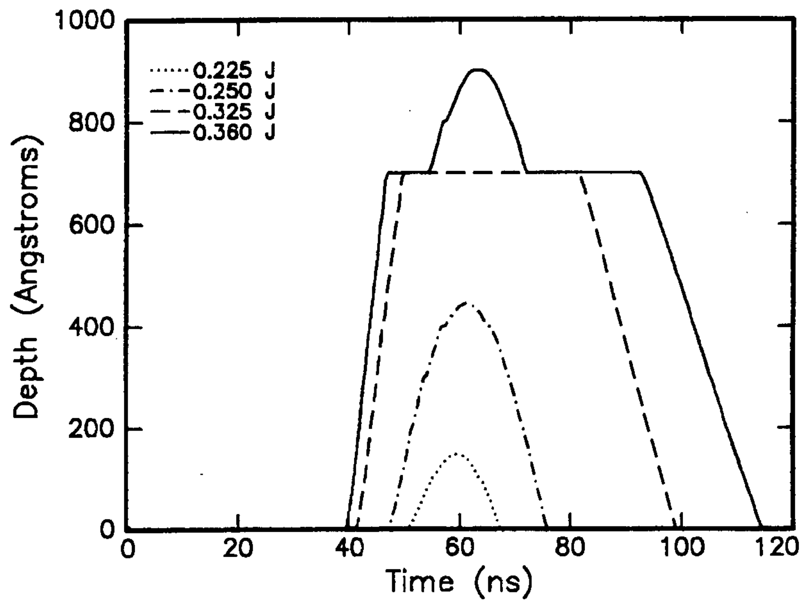

Figure 4.24: *Calculated liquid-solid interface position as a function of time for NiSi.*

Chapter 5

Conclusion

Through the course of this investigation it was shown that the Ni/Si<111> system most readily exhibited epitaxial behaviour. This was shown to be true for both thermally grown and laser assisted silicides.

Laser annealing of deposited metal layers yielded a very non-uniform silicide structure. This could be attributed to constitutional supercooling effects due to the large metal concentration gradient encountered by the moving liquid-solid interface. This large concentration gradient caused the melt front to become unstable and resulted in the formation of a cellular structure (not directly observed here). Thermal annealing of this structure resulted in the formation of a macroscopically non-uniform silicide-silicon interface.

In order to avoid constitutional supercooling effects; a layer of monosilicide was first grown thermally. This was then laser annealed and subsequently subjected to a further thermal anneal in order to remove any laser induced defects. The Ni/Si<111>, Ni/Si<100> and Co/Si<111> all showed near perfect single crystal minimum yields (~5%) while the best minimum yields achieved for the Co/Si<100> system were ~35%. These minimum yields were seen to be significantly lower than those of the thermally grown silicides. In general, the best epitaxy occured at laser energies that produced a silicide layer with a composition between that of the mono– and disilicides. It is thus thought that the laser induces liquid phase growth of an epitaxial disilicide in contact with the substrate and that the upper regions of the silicide layer contain metal and silicon atoms in equal quantities. This epitaxial layer then acts as a seed for further epitaxial growth in a later thermal anneal. It was also seen that the laser regions are laterally much more uniform than thermally grown

regions — the laser possibly reducing the random nature of the nucleation-controlled growth of the disilicides. Laser induced epitaxial regions were found to be mostly of the B Type orientation. The existence of a non-equilibrium *epitaxial monosilicide* was also noted. Mixed layers of Ni and Co were seen to be almost perfect single crystal on <111> substrates.

Numerical calculations of the laser annealing process, based on the conventional heat diffusion equation, were also performed. These were found to give fair quantitative agreement with those parameters that could be experimentally determined. The maximum undercooling at the liquid-solid interface was estimated to be $\sim$98 K for NiSi and $\sim$29 K for CoSi.

Although $CoSi_2$ and $NiSi_2$ have identical crystal structures and similar lattice constants, the issues and problems facing the epitaxial growth of these two silicides are very dissimilar. For the formation of thin silicide layers, a slight difference in lattice mismatch plays only a minor role. Therefore the observed difference of silicide reactions is probably attributable to other factors. One likely factor is the fundamental difference in the nature of the Ni-Si and Co-Si bond (metal atoms bond to the substrate in $CoSi_2$ whereas silicon atoms bond to the substrate in $NiSi_2$ [67]), which in turn leads to a difference in the energetics of the silicon-silicide interface. Another factor may be the dramatically different defect densities of the two crystals, leading to very different diffusivities at normal growth temperatures [68]. The larger residual resistivity of $NiSi_2$ is indicative of a high density of defects and/or a significant degree of disorder in the $NiSi_2$ lattice. Despite the difficulties presented by epitaxial growth of $CoSi_2$ on some silicon substrates; it is envisaged, in view of the superior electrical characteristics, that $CoSi_2$ will take preference in future applications of epitaxial silicides.

Appendix A

Green's Functions for the Heat Flow Problem

In order to solve the equation

$$\frac{\partial T(z,t)}{\partial t} = \frac{1}{\rho C}\frac{\partial}{\partial z}\left(K\frac{\partial T}{\partial z}\right) + \frac{(1-R)}{\rho C}\alpha I_o(t)e^{-\alpha z} \tag{A.1}$$

for various different physical situations it is convenient to begin with Greens function for a point like source. For the boundary conditions given 3.3 it is as follows [33]

$$\begin{aligned} G_o &= \frac{1}{\pi^{3/2}\rho C\beta^3}\, exp\left[-\frac{(x-x')^2+(y-y')^2}{\beta^2}\right] \\ &\cdot \sum_{n=-\infty}^{\infty}\left[exp\left(-\frac{(2nL-z-z')^2}{\beta^2}\right) + exp\left(-\frac{(2nL-z+z')^2}{\beta^2}\right)\right] \end{aligned} \tag{A.2}$$

where $\beta = 2(D|t-t'|)^{1/2}$ and the heat diffusivity $D = \frac{K}{\rho C}$ have been introduced. For future convenience the sum in A.2 with $z' = 0$ will be defined as Γ_1, where

$$\Gamma_1 = 2\sum_{n=-\infty}^{\infty} exp\left[-\frac{(2nL-z)^2}{\beta^2}\right]. \tag{A.3}$$

Green's function for any desired heat source geometry can now be constructed from equation (A.2). In the case of laser annealing we require a heat source with an energy density that decreases exponentially inside the material. In a material with absorption length α the appropriate Greens function is given by

$$G_1 = \alpha \int_0^L G_o e^{-\alpha z'}\, dz' = \frac{\alpha}{2\pi\rho C\beta^2}\, exp\left[-\frac{(x-x')^2+(y-y')^2}{\beta^2} - \frac{\alpha^2\beta^2}{4}\right]\Gamma_2$$

where

$$\Gamma_2 = \sum_{n=-\infty}^{\infty} exp[\alpha(2nL - z)] \cdot \left[erfc\left(\frac{(2n+1)L-z}{\beta}+\frac{\alpha\beta}{2}\right) - erfc\left(\frac{2nL-z}{\beta}+\frac{\alpha\beta}{2}\right)\right] + exp[-\alpha(2nL-z)] \cdot \left[erfc\left(-\frac{(2n+1)L-z}{\beta}+\frac{\alpha\beta}{2}\right) - erfc\left(-\frac{2nL-z}{\beta}+\frac{\alpha\beta}{2}\right)\right]. \quad (A.5)$$

This has now converted the heat source form a point into an "infinitely narrow" line source in the z direction. To describe heating by a lateral by (i.e. x, y) extended beam, the Greens function must now be integrated over the lateral beam distribution. If $f(r)$ is the radial irradiance profile (where $r^2 = x^2 + y^2$) the Green's function then becomes

$$G_2 = \left[2\pi \int_0^\infty f(r')\, dr'\right]^{-1} \int_0^\infty \int_0^{2\pi} G_1(r, r')\, f(r')\, r'\, dr'\, d\phi \quad (A.6)$$

(Note that G_1 would have to be converted to cylindrical co-ordinates where $(x-x')^2 + (y-y')^2 = r^2 + r'^2 - 2rr'\cos\phi$).

For a laser fitted with a beam homogeniser it would then be necessary to assume a laterally uniform source term i.e. $f(r)$ =constant. This however, represents an unphysical situation. It will lead to the first integral in equation (A.6) being infinite i.e. $f(r)$ is not normalisable. To circumvent this difficulty an infinite surface area S_∞ can be introduced, with the understanding that when the Greens function is used in equation (3.5) the term $P_a(t)/S_\infty$ must be replaced by the source intensity $I(t)$. If $f(r)$ =constant is inserted into equation (A.6), the resultant Greens function is as follows

$$G_{uniform} = \frac{1}{\sqrt{\pi}\rho C S_\infty \beta} \cdot \Gamma_1 \quad (A.7)$$

For a laser operating in the fundamental mode (TEM_{00}) and not fitted with a beam ho-

mogeniser, the lateral beam profile is Gaussian. We can then set $f(r) = e^{-r^2/w^2}$ where w is the so-called beam width. If this $f(r)$ is inserted into equation (A.6), the integral then yields

$$G_{gaussian} = \frac{1}{2\pi\rho C(\beta^2 + w^2)}\, exp\left(-\frac{r^2}{\beta^2 + w^2} + \frac{\alpha^2\beta^2}{4}\right)\Gamma_2. \qquad \text{(A.8)}$$

Now either $G_{uniform}$ or $G_{gaussian}$ can be inserted into equation (3.5) along with the temporal evolution of the incident pulse and then the complete temperature distribution can be found.

Appendix B

Optical Properties of Si; Ni, Co and their silicides at 694nm

	Reflctivity (R)	Absorption coeff (α) (cm^{-1})	Absorption length (α^{-1}) (Å)
Si (cryst)	$0.324 + 4\times10^{-5}T$ (for T<1000K) $0.584 - 4.8\times10^{-4}T + 2.6\times10^{-7}T^2$ (for T≥1000K) [69]	1340 exp(T/427) for T≤1685K [83]	36960[a]
Si (amorph)	$0.334 + 1.2\times10^{-4}T$ [71]	7×10^4	1429
Si (liquid)	0.72 [72]	1×10^6 [72]	100
Ni	0.71 [73]	7.26×10^5 [85]	138
NiSi	0.48 [73]	4.94×10^5 [75]	202
$NiSi_2$	0.42 [75]	3.75×10^5 [75]	267
Co	0.68 [76]	7.11×10^5 [76]	141
CoSi	0.47 [b] [77]	4×10^5 [c]	250
$CoSi_2$	0.31 [76]	2.96×10^5 [76]	338

[a]evaluated at 300K
[b]at 643nm
[c]estimated value

Appendix C

Thermal Properties of Si; Ni, Co and their silicides

	Density (ρ) (g cm^{-3})	Melting Temp. (T_m) (K)	Latent Heat (ΔH) [a] (J g^{-1})	Thermal Conductivity (K) (W cm^{-1} K^{-1})	Specifc Heat Capacity (C_p) (J g^{-1} K^{-1})
Si (cryst)	2.33 [78]	1685	1740	$1585 \times T^{-1.23}$ (for $300<T\leq1370K$) 0.221 (for $T>1370K$) [79]	$(1.978 + 3.54 \times 10^{-4}T - 3.68 \times 10^{4}T^{-2})/\rho$ [80]
Si (amorph)	2.33	1420 [81]	1320 [82]	$1.3 \times 10^{-11} \times (T-900)^3 + 1.3 \times 10^{-9} \times (T-900)^2 + 1.0 \times 10^{-6} \times (T-900) + 0.01$ [83]	$(1.978 + 3.54 \times 10^{-4}T - 3.68 \times 10^{4}T^{-2})/\rho + 1.71 \times 10^{-1}T/1685 - 7.97 \times 10^{-3}$
Si (liquid)	2.52 [78]	N/A	N/A	0.221 [79]	0.950

[a]Latent Heat of fusion

	Density (ρ) (g cm^{-3})	Melting Temp. (T_m) (K)	Latent Heat (ΔH) [a] (J g^{-1})	Thermal Conductivity (K) (W cm^{-1} K^{-1})	Specifc Heat Capacity (C_p) (J g^{-1} K^{-1})
Ni	8.90 [84]	1728 [85]	297.6 [85]	$1.547 - 2.89\times10^{-3}T + 3.03\times10^{-6}T^2 - 9.51\times10^{-10}T^3$ (for T<1400K) 0.80 (1400≤T<1728K) 0.749 (for T≥1728K) [85][b]	0.444 [85]
NiSi	6.56 [c] [84]	1273 [84]	512 [86]	0.208 [87]	$0.620 + 4.33\times10^{-5}T - 1.11\times10^{4}T^{-2}$ (for T≤1273) 0.992 (for T>1273) [88]
$NiSi_2$	4.86 [84]	1266 [84]	601 [88]	$0.185 - 2.919\times10^{-4}T + 1.208\times10^{-7}T^2$ (for T<1266) 0.0099 (for T≥1266) [85][b]	$0.683 + 9.626\times10^{-5}T - 9.426\times10^{3}T^{-2}$ (for T≤1266) 0.935 (for T>1266) [88]
Co	8.71 [85]	1766 [85]	274.7 [85]	1.00 [84]	$0.289 + 5.15\times10^{-4}T - 2.67\times10^{-7}T^2$ (for T≤650K) 0.52 (for T>650K) [85][b]
CoSi	6.57 [84]	1733 [84]	769 [86]	0.137 [88]	$0.472 + 1.37\times10^{-4}T - 6.529\times10^{3}T^{-2}$ (for T≤1733) 1.006 (for T>1733) [88]
$CoSi_2$	4.95 [84]	1599 [84]	869 [88]	0.151 [84]	$0.622 + 1.314\times10^{-4}T - 8.24\times10^{3}T^{-2}$ (for T≤1599) 1.007 (for T>1599) [88]

[a] Latent Heat of fusion

[b] own fit to empirical data

[c] but $\rho = 5.86$ g/cm^3 for orthorhombic structure

Appendix D

SEM Micrographs

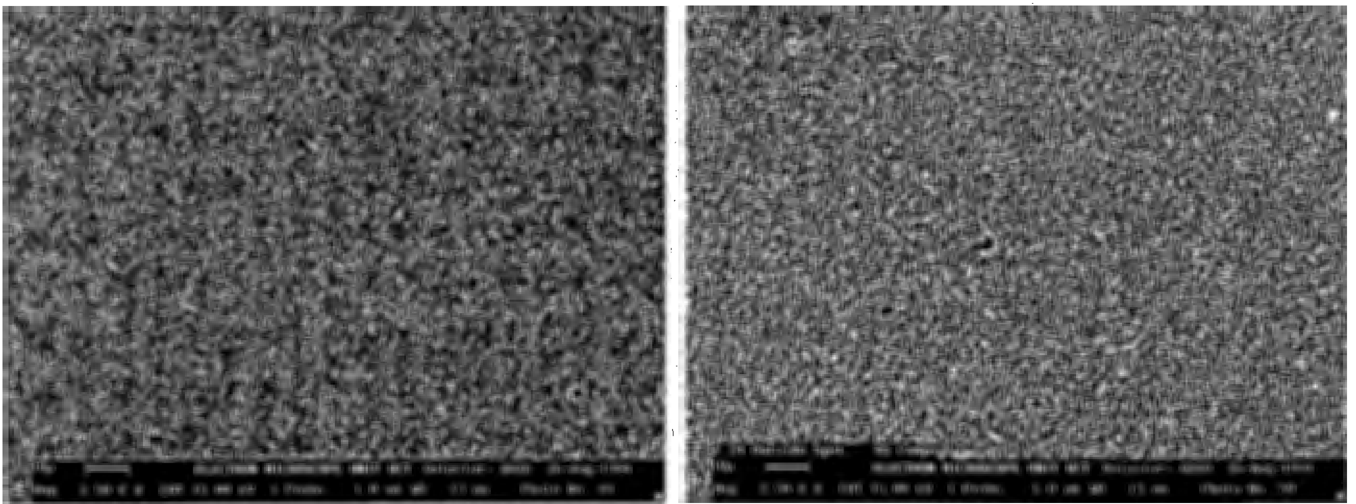

Figure D.1: *Backscattered electron images taken inside (left) and outside (right) of the laser spot for Ni-Si*<111>.

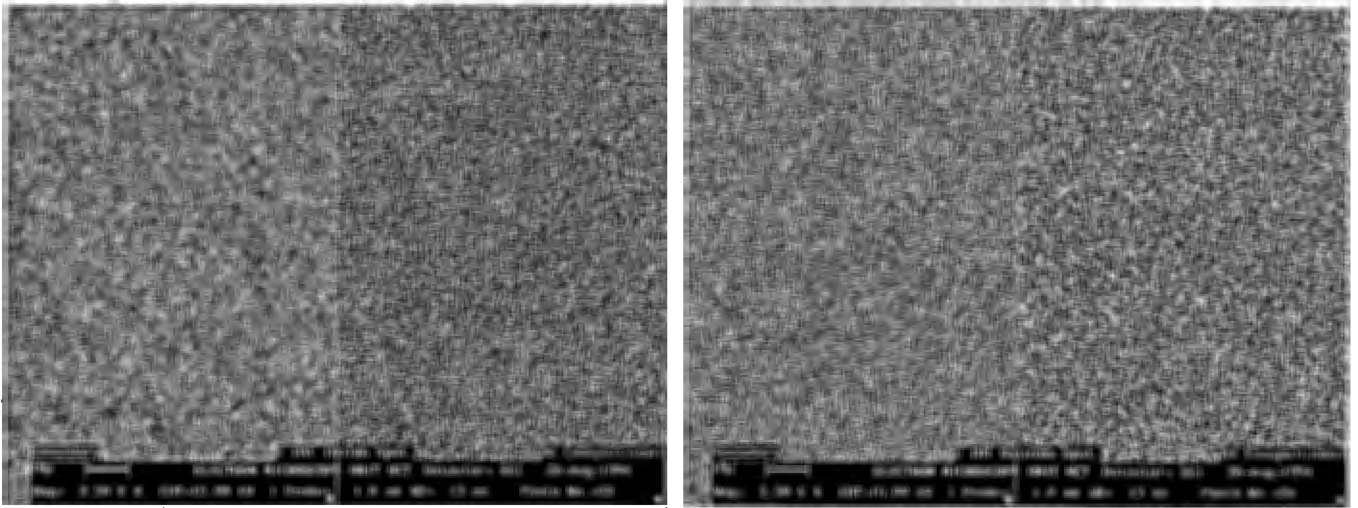

Figure D.2: *Backscattered and secondary electron images taken inside (left) and outside (right) of the laser spot for Ni-Si*<100>.

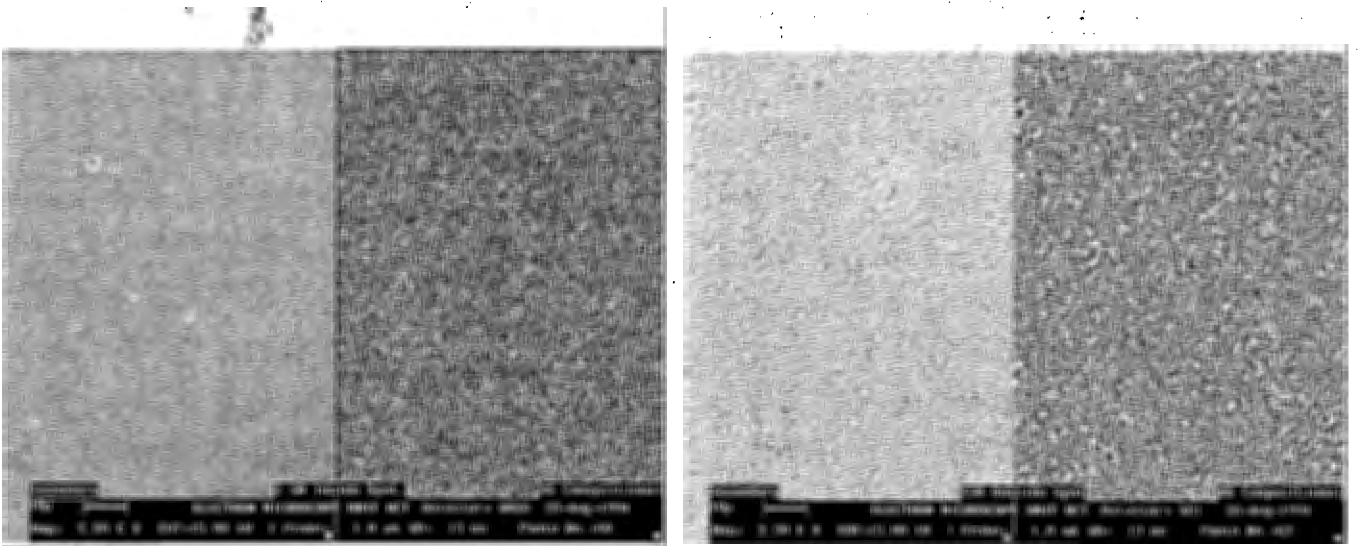

Figure D.3: *Backscattered and secondary electron images taken inside (left) and outside (right) of the laser spot for Co-Si*<100>.

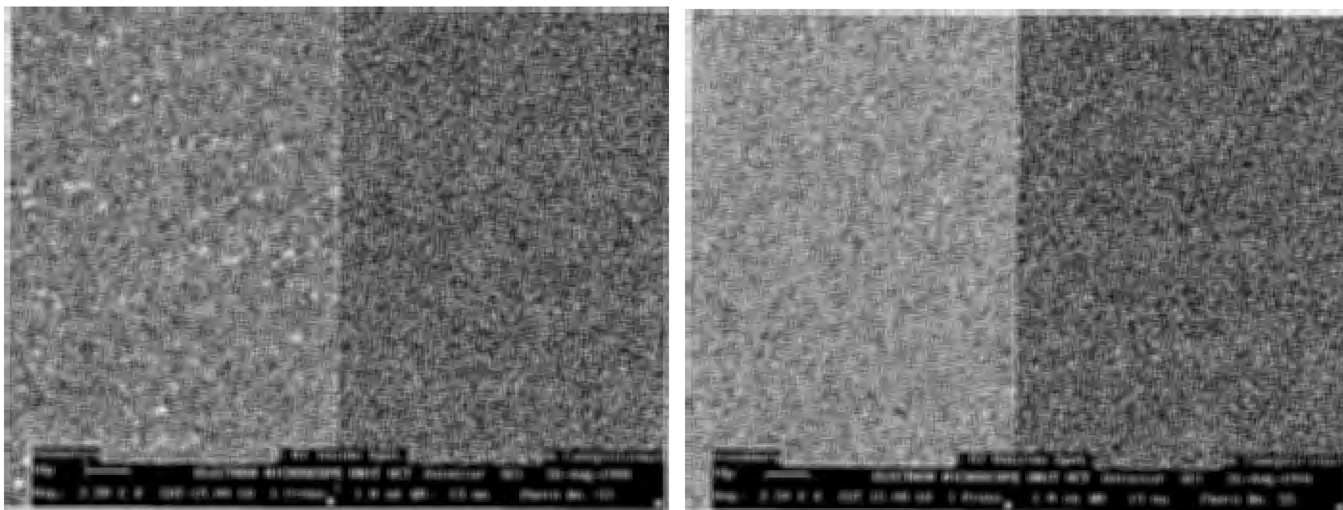

Figure D.4: *Backscattered and secondary electron images taken inside (left) and outside (right) of the laser spot for Co-Si*<111>.

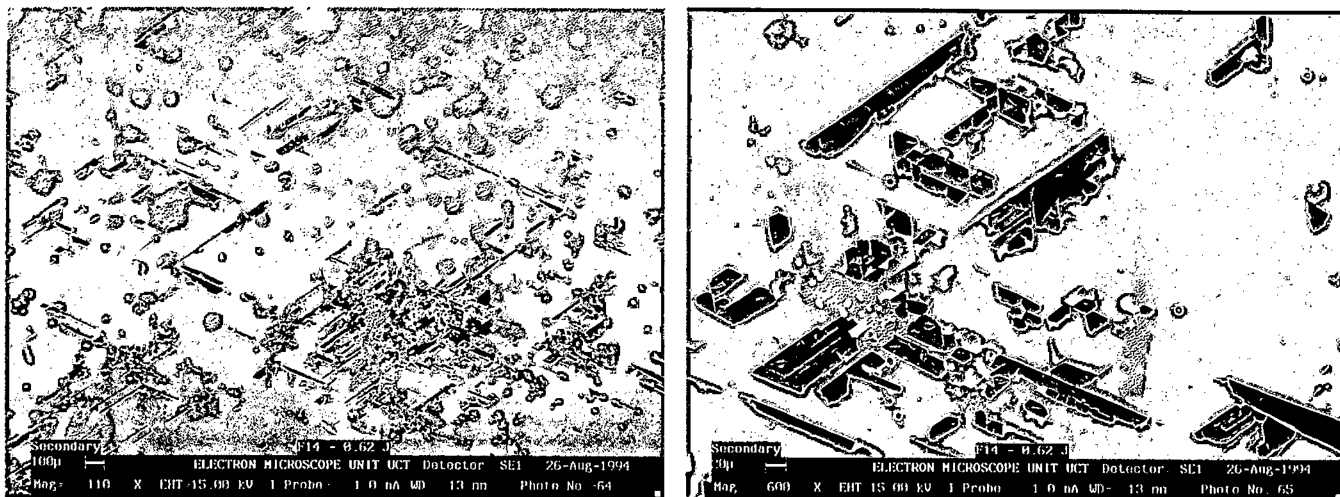

Figure D.5: *Damaged CoSi after laser annealing at high energies.*

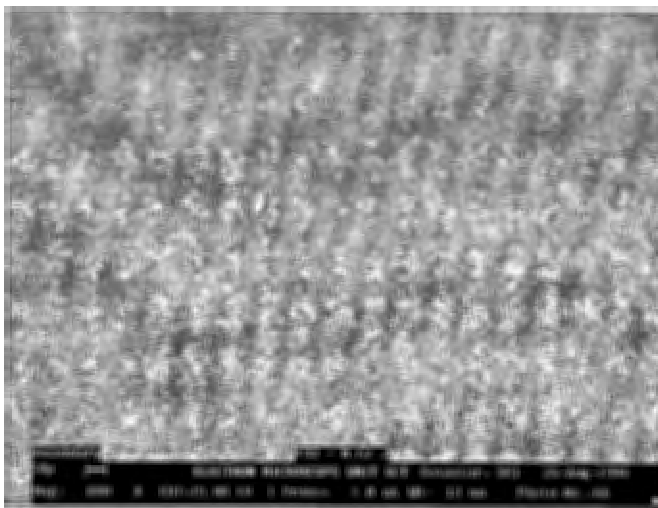

Figure D.6: *NiSi after being annealed at the same energy as the CoSi above. No large scale damage is evident.*

Appendix E

Thermodynamics of the Ni–Si and Co–Si Systems

Shown below are the phase diagrams of the Ni–Si and Co–Si systems [89]. It should be emphasised that these are *equilibrium* phase diagrams and also that the laser annealing process is certainly not an equilibrium one. During laser annealing the surface (top few hundred Angstroms) is "far from equilibrium" and the standard phase diagrams are strictly no longer valid. However, the equilibrium phase diagrams can still be used as a *qualitative guide* for understanding the formation of various phases. Since the best results were obtained with a monosilicide on the substrate, only that case will be briefly discussed.

Nickel–Silicon : If the laser pulse does not melt the NiSi all the way through to the substrate, then the resulting liquid will resolidify into the solid since NiSi is a congruent compound. However, if the pulse has sufficient energy to melt through to the substrtate and the concentration of Si in the liquid reaches 56% then upon cooling the liquid undergoes a eutectic reaction and forms NiSi and $\alpha NiSi_2$. If the concentration of silicon in the liquid is able to reach 59% then the liquid will undergo a peritectic reaction with solid silicon and form $\beta NiSi_2$. Upon further cooling this form of $NiSi_2$ converts to the more stable $\alpha NiSi_2$. For silicon concentrations greater than 59%, the liquid will "segregate out" solid silicon and move along the liquidus until a concentration of 59% Si is reached; the liquid will then undergo the aforementioned peritectic reaction.

Cobalt–Silicon : For low pulse energies that do not melt the CoSi all the way down to the substrate, the liquid will resolidify as CoSi. However, since CoSi is not a line compound the resulting solid will not necessarily be homogeneous in the silicon concentration; but *on average* the resulting compound will have the same stochiometry as the initial CoSi. If the melt front does penetrate the substrate, then at a Si concentration of 62% the liquid undergoes a eutectic reaction forming CoSi and $CoSi_2$. For Si concentrations of 78% the liquid undergoes another eutectic reaction and forms (solid) Si and $CoSi_2$. For concentrations between these values the liquid will "segregate out" the closest solid and then move along the liquidus until one of the two eutectic points (at 78 and 62% Si) is reached.

These qualitative observations at least agree with the experimental results (i) for low energies the monosilicide is unaffected (ii) for medium energies both mono– and dislicide are formed and (iii) for high energies only the disilicide is formed.

Figure E.1: *Nickel- Silicon (equilibrium) phase diagram.*

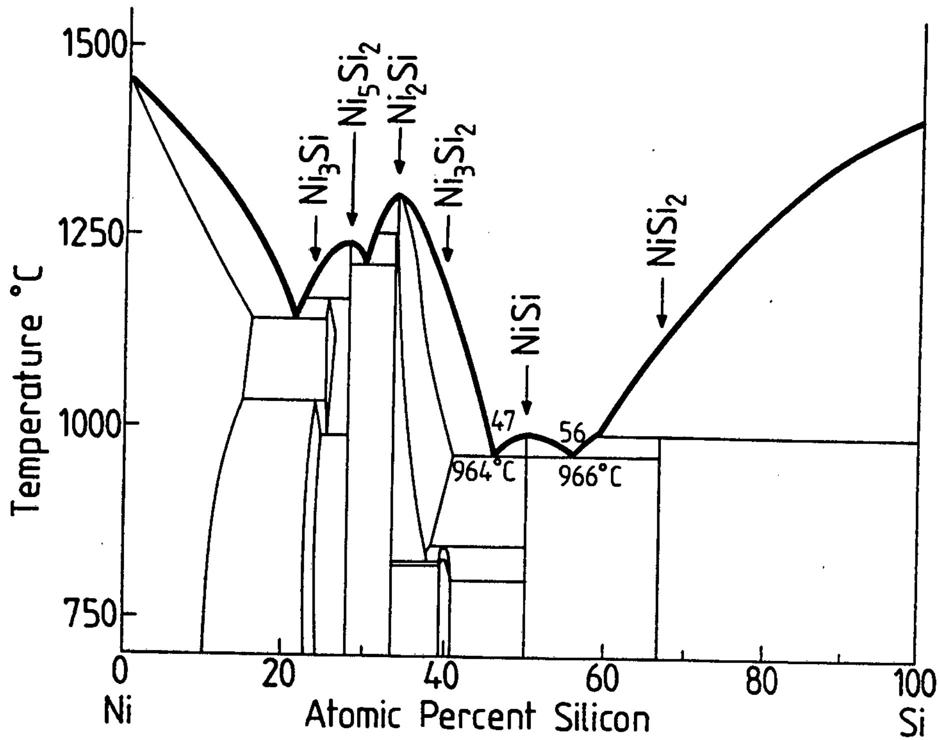

Figure E.2: *Cobalt–Silicon (equilibrium) phase diagram.*

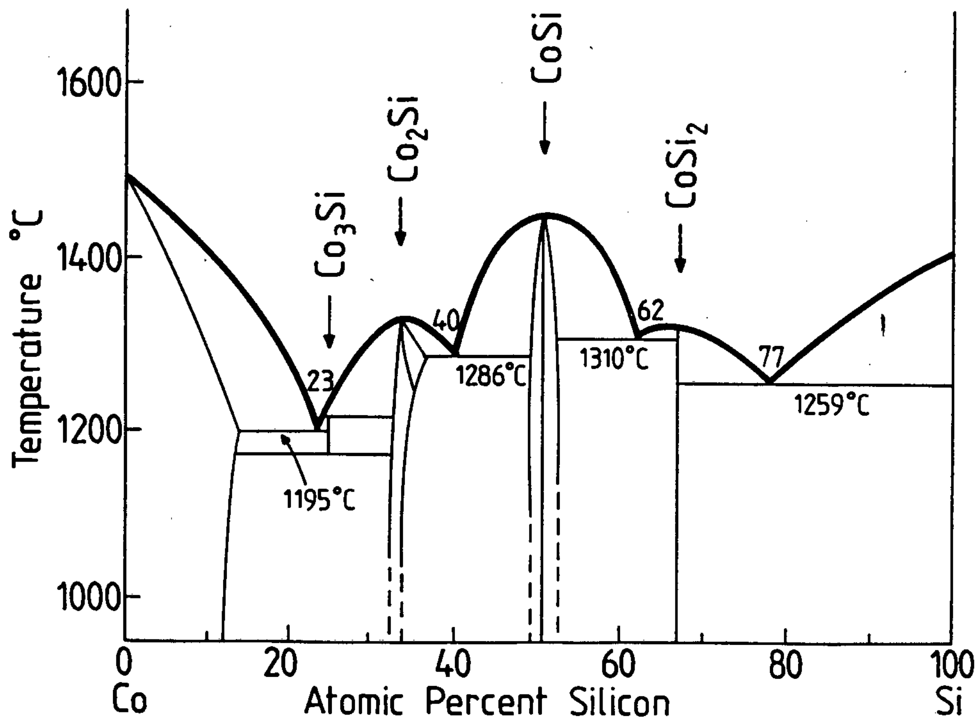

Bibliography

[1] J.P. Sullivan, R.T. Tung, D.J. Eaglesham, F. Schrey, W.R. Graham; *J. Vac. Sci. Technol. B.*, **11**(4), 1564 (1993)

[2] W.E. Spicer, I. Lindau, P. Sheath, C.Y. Su, P.W. Chye; *Phys. Rev. Lett.*, **44**, 420 (1980)

[3] J. Tersoff; *Phys. Rev. Lett.*, **52**, 465 (1984)

[4] T. Kawamu, D. Shimoda, H. Muto; *Appl. Phys. Lett.*, **11**, 101 (1967)

[5] Y.S. Chang, J.J. Chu, L.J. Chen; Thin Films : Interfaces and Phenomena; R.J. Nemanich, P.S. Ho, S.S. Lau (Ed's); *Mater. Res. Soc. Symp. Proc.*, **54**, 57 (1986)

[6] L.J. Chen, H.C. Cheng, W.T. Lin; Thin Films : Interfaces and Phenomena; R.J. Nemanich, P.S. Ho, S.S. Lau (Ed's); *Mater. Res. Soc. Symp. Proc.*, **54**, 245 (1986)

[7] C.A. Hill, P. Hunt; *Nucl. Instrum. Methods B*, **55**, 1 (1991)

[8] P.B. Allen, W.W. Schulz; *Phys. Rev. B*, **47**, 14434 (1993)

[9] D. Uffmann, S. Zaage; *Appl. Phys. Lett.*, **63**, 3179 (1993)

[10] P.A. Badoz, D. Bensahel, L. Guerin, C. Puissant, J.L. Regalini; *Appl. Phys. Lett.*, **56**, 2307 (1990)

[11] A.K. Antonenko, N.N. Gerasimenko, A.V. Dvurechensky, L.S. Smirnov, G.M. Tseitlin; *Sov. Phys.-Semicond.*(Engl. Transl.), **10**, 81 (1976)

[12] A.G. Cullis, H.C. Webber, P. Bailey; *J. Phys. E: Sci. Instrum.*, **12**, 688 (1979)

[13] W.K. Chu, J.W. Mayer, M.A. Nicolet; *Backscattering Spectrometry*, Academic Press, Orlando, 1978

[14] P.P. Pronko, B.R. Appleton, O.W. Holland, S.R. Wilson; *Phys. Rev. Lett.*, **43**, 779 (1979)

[15] O.H. Crawford; *Phys. Rev. Lett.*, **44**, 185 (1980)

[16] K.S. Harshavardhan, R.S. Yalamanchi, L.K. Roo; *Appl. Phys. Lett.*, **55**(4), 351 (1989)

[17] K.N. Tu, K.Y. Ahn, S.R. Herd; *Appl. Phys. Lett.*, **39**(11), 927 (1981)

[18] T. Takuyama; *Laser and Electron Beam Processing of Materials*, C.W. White, P.S. Peercy (Ed's), Academic, New York, 1980

[19] J.M. Poate, J.C. Bean; *Laser Annealing of Semiconductors*, J.M. Poate, J.W. Mayer (Ed's), Academic, New York, 1982

[20] J.M. Poate, H.J. Leamy, T.T. Sheng, G.K. Celler; *Appl. Phys. Lett.*, **33**, 918 (1978)

[21] C.F. Bohren, D.R. Huffman; *Absorption and Scattering of Light by Small Particles*, Wiley, New York, 1983

[22] J.A. van Vechten, R. Tsu, F.W. Saris, D. Hoonhaut; *Phys. Lett. A*, **74**, 417 (1979)

[23] P. Baeri, S.U. Campisano, G. Foti, E. Rimini; *J. Appl. Phys.*, **50**, 788 (1979)

[24] J.C. Wang, R.F. Wood, P.P. Pronko; *Appl. Phys. Lett.*, **33**, 455 (1978)

[25] J.M. Gibson, R. Tsu; *Appl. Phys. Lett.*, **37**(2), 197 (1980)

[26] R. Biswas, V. Ambegaokar; *Phys. Rev. B*, **26**, 1980 (1982)

[27] G.J. Galvin, M.O. Thompson, J.W. Mayer, R.B. Hammond, N. Paulter, P.S. Peercy; *Phys. Rev. Lett.*, **48**(1), 33 (1982)

[28] R.F. Wood, G.E. Giles; *Phys. Rev. B*, **23**, 2923 (1981)

[29] R.F. Wood, J.R. Kirkpatrick, G.E. Giles; *Phys. Rev. B*, **23**, 5555 (1981)

[30] R.F. Wood; *Phys. Rev. B*, **25**, 2786 (1982)

[31] R.E. Harrington; *J. Appl. Phys.*, **38** 3266 (1967)

[32] D.M. Kim, R.R. Shah, D.L. Crosthwait; *Laser and Electron Beam Processing of Materials*, C.W. White and P.S. Peercy (Ed's), Academic, New York, 1980

[33] H.S. Carlslaw, J.C. Jaeger; *Conduction of Heat in Solids*, 2nd Ed., Oxford University Press, Oxford, 1959

[34] K.A. Jackson, B. Chalmers; *Can. J. Phys.*, **34**, 473 (1956)

[35] D. Turnbull; *Solid State Phys.*, **3**, 225 (1956)

[36] J.Q. Broughton, G.H. Gilmer, K.A. Jackson; *Phys. Rev. Lett.*, **49**, 1496 (1982)

[37] F.F. Abraham, J.Q. Broughton; *Phys. Rev. Lett.*, **56**, 734 (1986)

[38] K.A. Jackson; *Can. J. Phys.*, **36**, 683 (1958)

[39] M. von Allmen; Laser-Solid Interactions and Transient Thermal Processing of Materials; J. Narayan, W.L. Brown, R.A. Lemons (Ed's); *Mat. Res. Soc. Symp. Proc.*, **13**, 691 (1983)

[40] F. Spaepen, D. Turnbull; *Laser Annealing of Semiconductors*, J.M. Poate, J.W. Mayer (Ed's), Academic, New York, 1982

[41] S.E. Kroonin; *Computational Physics*, Benjamin Cummings, Menlo Park CA, 1986

[42] R.F. Wood, G.A. Geist; *Phys. Rev. B*, **34**, 2606 (1986)

[43] V. Hinkel, L. Sorba, H. Haak, K. Horn; *Appl. Phys. Lett.*, **50**, 1257 (1987)

[44] K.C.R. Chiu, J.M. Poate, J.E. Rowe, T.T. Sheng, A.G. Cullis; *Appl. Phys. Lett.*, **38**, 988 (1981)

[45] F.M. d'Heurle; *Thin Solid Films*, **105**, 285 (1983)

[46] J. Narayan, H. Naramoto, C.W. White; *J. Appl. Phys.*, **53**, 912 (1982)

[47] M. von Allmen, S.S. Lau, T.T. Sheng, M. Wittmer; *Laser and Electron Beam Processing of Materials*, C.W. White, P.S. Peercy (Ed's), Academic, New York, 1980

[48] G.J. van Gurp, G.E.J. Eggermont, Y. Tamminga, W.T. Stacy, J.R.M. Gijsbers; *Appl. Phys. Lett.*, **35**, 237 (1979)

[49] M.G. Grimaldi, P. Baeri, E. Rimini, G. Cellati; *Appl. Phys. Lett.*, **43**, 244 (1983)

[50] C.M. Comrie, V. Hoffman; *S. Afr. J. Phys.*, **16**, 171 (1993)

[51] R.T. Tung, J.M. Gibson, D.C. Jacobson, J.M. Poate; *Appl. Phys. Lett.*, **43**, 476 (1983)

[52] F.M. d'Heurle, C.S. Peterson; *Thin Solid Films*, **128** 283 (1985)

[53] F.M. d'Heurle, C.S. Peterson, L. Stolt, B. Stritzker; *J. Appl. Phys.*, **53**, 5678 (1982)

[54] S.S.Lau, N.W. Cheung; *Thin Solid Films*, **71**, 117 (1980)

[55] R.T. Tung; *Mat. Chem. Phys.*, **32**, 107 (1992)

[56] M. Lawrence, A. Daas, D.B. Fraser, C-S. Wei; *Appl. Phys. Lett.*, **58**, 1308 (1991)

[57] R.A. Hamm, J.M. Vandenberg, J.M. Gibson, R.T. Tung; Layered Structures, Epitaxy and Interfaces; J.M. Gibson, L.R. Dawson (Ed's); *Mat. Res. Soc. Symp. Proc.*, **37** 367 (1985)

[58] D. Hesse, R. Mattheis; *Phys. Stat. Sol. (a)*, **116**, 67 (1989)

[59] G. Bai, D.N. Jamieson, M.A. Nicolet, T. Vreeland; Epitaxy of Layered Semiconductor Structures; R.T. Tung, L.R. Dawson, R.L. Gunshor (Ed's); *Mat. Res. Soc. Symp. Proc.*, **102**, 259 (1988)

[60] C.M. Comrie, V. Hoffman; to be published in *Mat. Res. Soc. Symp. Proc.*, Winter Conference, Boston, 1993

[61] P. Baeri, M.G. Grimaldi, F. Priolo, A.G. Cullis, N.G. Chew; *J. Appl. Phys.*, **66**, 861 (1989)

[62] P. Villars, L.D. Calvent (Ed's); *Pearson's Handbook of Crystallographic Data for Intermetallic Phases*, American Society for Metals, Ohio, 1985

[63] J.M. Gibson, J.L. Batstone, R.T. Tung; *Appl. Phys. Lett.*, **51**, 45 (1987)

[64] K.A. Madar, H. von Kanel, A Baldereschi; *Phys Rev B*, **48**, 4364 (1993)

[65] T.G. Finstad, D. Anfiteatra, V. Deline, F.M. d'Heurle, P. Gas, V. Moruzzi, K. Schwarz, J. Tersoff; *Thin Solid Films*, **135**, 229 (1986)

[66] G.J. Galvin, J.W. Mayer, P.S. Peercy; *Appl. Phys. Lett.*, **46**, 644 (1985)

[67] P.J. van den Hoek, W. Ravenek, E.J. Baerends; *Phys. Rev. Lett.*, **60** 1743 (1988)

[68] O. Thomas, P. Gas, A. Charai, F.K. Le Goues, A. Michel, G. Scilla, F.M. d'Heurle; *J. Appl. Phys.*, **64**, 2973 (1988)

[69] M. Toulemonde, R. Heddache, F.Nielsen, P. Siffert; *J. Appl. Phys.*, **56**, 1878 (1984)

[70] G.E. Jellison Jr., F.A. Modine; *Appl. Phys. Lett.*, **41**, 180 (1982)

[71] F.G. Allen; *J. Appl. Phys.*, **28**, 1510 (1957)

[72] K.M. Sharev, B.A. Baum, P.V. Gel'd; *Sov. Phys. Solid State*, **16**, 2111 (1975)

[73] W. Henrion, H. Lange; *Phys. Stat. Sol. (b)*, **112**, K57 (1982)

[74] D.R. Lide(Ed); *CRC Handbook of Chemistry and Physics*, 74th Ed., CRC Press, 1993/4

[75] M. Amiotti, A. Borghesi, G. Guizzetti, F. Nava; *Phys. Rev. B.*, **42**(14), 8939 (1990)

[76] C. Viguier, A. Cros, A. Humbert, C. Ferrieu, O. Thomas, R. Madar, J.P. Senateur; *Sol. Stat. Comm.*, **60**(12), 923 (1986)

[77] K.N. Tu, K.Y. Ahn, S.R. Herd; *Appl. Phys. Lett.*, **39**(11), 927 (1981)

[78] R.O. Bell, M. Toulemonde, P. Siffert; *Appl. Phys. Lett.*, **19**, 313 (1979)

[79] A. Goldsmith; *Handbook of Thermophysical Properties of Solid Materials*, Macmillan, New York, (1961)

[80] R.C. Weast(Ed); *CRC Handbook of Chemistry and Physics*, 63rd Ed., CRC Press, 1982/3

[81] J.M. Poate; *Nucl. Instrum. Methods B*, **209**, 211 (1983)

[82] D.H. Lowndes, C.W. Wood, J. Narayan; *Phys. Rev. Lett.*, **52**, 7 (1984)

[83] G.E. Jellison, F.A. Modine; *Appl. Phys. Lett.*, **41**, 180 (1982)

[84] M.A. Nicolet, S.S. Lau; *Formation and Characterisation of Transition-Metal Silicides in VLSI Electronics — Microstructure Science*, **6**, N.G. Einspruch, G.B. Larrabee (Ed's), Academic, New York, 1983

[85] D.R. Lide(Ed), *CRC Handbook of Chemistry and Physics*, 74th Ed., CRC Press, 1993/4

[86] Private communication from Prof M. Olmstead, Physics Dept, Univ of Washington, Seattle, USA

[87] Y.S. Toulokian; *Thermophysical Properties of High Temperature Solid Materials*, Macmillan , 1967

[88] Private communication from Dr Andre Witzmann based on information in:
G.W. Smasnov et. al.; *Silicides*, Metallurgia, Moscow, 1979
P.W. Geld; *Transition Metal Silicides of Group IV*, Metallurgia, Moscow, 1986

[89] T.B. Massalski (Editor), *Binary Alloy Phase Diagrams (2nd Ed)*, American Society of Metals, Ohio, 1990